The Hong Kong Polytechnic University
mechanical engineering

THREE-DIMENSIONAL VORTICAL STRUCTURES BEHIND A NORMAL OR INCLINED CYLINDER WITH OR WITHOUT RUNNING WATER RIVULETS

Jiefeng Huang

A thesis submitted in partial fulfilment of the requirements for the Degree of Master of Philosophy

Department of Mechanical Engineering
The Hong Kong Polytechnic University

October, 2005

Certificate of Originality

I hereby declare that this thesis is my own work and that, to the best of my knowledge and belief, it reproduces no material previously published or written, nor material that has been accepted for the award of any other degree or diploma, except where due acknowledgement has been made in the text.

________________ (Signed)

Huang Jiefeng

October, 2005

Abstract

As a step to identify the excitation mechanism of rain-wind induced cable vibration, three-dimensional vortical structures have been measured in a circular cylinder wake using Particle Imaging Velocimetry (PIV) for the Reynolds number range of 2 x 10^3 to 1 x 10^4. The PIV was modified, compared with the conventional one, in terms of its light sheet arrangement to capture reliably streamwise vortices. While in agreement with previous reports, the presently measured spanwise structures complement the data in the literature in the streamwise evolution of the near-wake spanwise vortex in size, strength, streamwise and lateral convection velocities, shedding new light upon vigorous interactions between oppositely signed spanwise structures. The longitudinal vortices display mushroom patterns in (x, z)-plane, where x represents free flow direction and z is in line with cylinder axis, in the immediate proximity to the cylinder. Their most likely inclination in the (x, y)-plane, where y is perpendicular to both x and z directions, is inferred from the measurements in different (x, z)-planes. The longitudinal vortices in the (y, z)-plane show alternate change in sign, though not discernible at $x/d > 15$, where d is the diameter of cylinder. They decay in the maximum vorticity and circulation rapidly from $x/d = 5$ to 10 and slowly for $x/d > 10$, and are further compared with the spanwise vortices in size, strength and rate of decay. Then the effects of water rivulets running along an inclined circular cylinder on the near-wake were experimentally investigated. Water was released from the upper end of the cylinder at a volume flow rate Q. At an incoming wind speed $U_\infty = 8 – 15$ m/s, two water rivulets were observed near the flow separation points, running along the cylinder inclined at $\alpha = 45°$ for $0° \leq \beta \leq 90°$, where β is the cylinder yaw angle, and both oscillating circumferentially. The quasi-periodical vortex street is observed intermittently with and without the presence of the rivulets. The rivulets lead to a significant increase in the drag coefficient, which is consistent with the violent vibration associated with the rain-wind-structure interactions. It is found that the vortex strength grows by up to 60% as β increases from 0° to 30°. A mechanism for the rain-wind-induced cable vibration is proposed.

LIST OF PUBLISHED, ACCEPTED OR SUBMITTED PUBLICATIONS

J.F. Huang, Y. Zhou, T. Zhou, Three-dimensional wake structure measurement using a modified PIV technique, accepted by Experiments in Fluids. Feb. 2006

Z.J. Wang, Y. Zhou, Y.L. Xu, **J.F. Huang**, Water rivulet effects on the near wake of an inclined cylinder, Proceeding of International Conference on Flow-induced Vibration, 2004, Paris France, Vol. 2, pp. 449-454, 2004.

Z.J. Wang, Y. Zhou, **J.F. Huang**, Y.L. Xu, Fluid dynamics around an inclined cylinder with running water rivulets, Journal of Fluids and Structures, Vol. 21, pp. 49-64, 2005.

J.C. Hu, Y. Zhou and **J.F. Huang**, Measurement of the corner effects of a square prism on the near wake using an on-line phase-locked PIV technique, Proceeding of the Fourth European&Africa Conference on Wind Engineering, 2005, Prague, paper #317.

J.C. Hu, Y. Zhou and **J.F. Huang**, INVARIANCE OF C_DS_T IN THE TURBULENT WAKE OF BLUFF BODIES, Proceedings of 2005 ASME Fluids Engineering Division Summer Meeting and Exhibition, 2005, Houston, TX, USA, paper #FEDSM2005-77046.

Acknowledgements

I would like to express great thanks to my supervisor, Dr. Zhou Yu, who guides me into my research area of rain-wind induced vibration during my Mphil. study, and let me know what research is all about. His kindness, patience, encouragement and support make this thesis possible. Without his generous help during the past two years, the project cannot be finished. During the past two years, I experienced the transfer from an undergraduate to a postgraduate with a comprehension about what characteristics a researcher should have, and it has a great influence on my future academic exploration.

I would also like to thank Mr. Hu J.C. and Zhang M.M. for their kindly help and support during the past two years, and Mr. K.K. Lo and Mr. K.H. Hui for their allocation and preparation of experiment facilities.

Finally, I am forever indebted to my parents and my wife Fu Shan for their unconditional understanding, endless patience and encouragement. Without their sacrifice, support and deep love, I cannot successfully finish my former studies and pursue further education.

Table of Contents

List of Figures

Chapter 1: Introduction

1.1 Introduction to rain-wind induced vibration

Long and flexible cables in modern cable-stayed bridges are inherently of low damping and are susceptible to vibration in a cross wind due to fluid excitation forces associated with vortex shedding from the cables. In the presence of rain, oscillating and moving water rivulets occur along a cable. The ensuing aero-hydro-elastic interaction between cable, wind and oscillating water rivulets results in a grossly amplified cable vibration within a certain range of wind speeds and restricted large vibration amplitudes. This specific cable vibration under the combined influence of wind and rain is named as rain-wind-induced cable vibration or rain-wind-induced vibration. The vibration, for most of the time, occurs for a wind speed from 8 to 15 m/s and at a yaw angle of β = 20˚ - 60˚; it is always associated with water rivulets running along the cable and oscillating circumferentially. In general, two water rivulets are formed, occurring on the lower windward side and upper leeward side of the cable, respectively. The upper rivulet on the leeward side has been identified to be largely responsible for the rain-wind-induced cable vibration, while the other one on the windward side has a negligible effect (Bosdogianni & Olivari 1996).

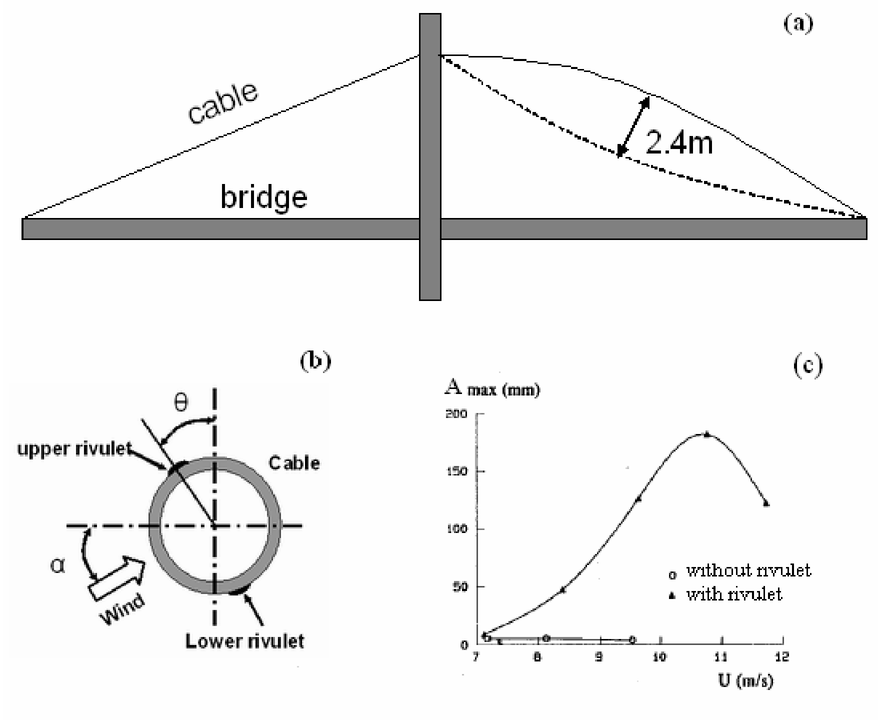

Figure 1.1 : (a) illustration of bridge cables in the states of stable (left) and rain-wind induced vibration (right), (b) scheme of cable cross-section with water rivulets on surface, (c) comparison of cable vibration amplitudes vs. wind velocity with and without rivulet, obtained by Flamand (1995).

Hikami and Shiraishi (1988) gave the first report of the rain-wind-induced vibration of stay cables associated with the Meikonishi bridge in Japan. Since then, the observation of the rain-wind-induced cable vibration has been reported for a number of long span bridges in Japan, China, and countries in Europe and North America. The rain-wind-induced cable vibration may have maximum peak-to-peak amplitude up to 2.4m in moderately windy and rainy days (Matsumoto *et al.* 1998), thus shorting the fatigue life of the cable and cable joint parts, and even causing damages of cables, dampers and wires connecting cables (Matsumoto *et al.* 2001a) and affecting the safety of entire bridge. This problem has become a great concern to bridge and wind engineering communities, and has induced many field observations and experimental investigations, including present work, conducted in wind tunnels with various cable models.

1. 2 Literature Review: possible exciting mechanisms of cable vibration

There are a few fluid-induced vibration mechanisms that may cause long bridge cables of low structural damping vibrate under the force of wind, such as the well known Karman vortex excitation, wake galloping instability (Ruscheweyh 1983), galloping instability (Den Hartog 1956) *etc*. Interest in understanding the mechanisms of the rain-wind-induced cable vibration has kept growing in the past decade; both field measurements and wind tunnel tests with simulated rain conditions have been vigorously pursued.

1.2.1 Karman vortex shedding and lock-in phenomenon

When a cylinder of diameter d is immersed in a laminar flow moving at velocity U, regular Karman vortices shed from two sides of the cylinder alternatively at shedding frequency f_s.

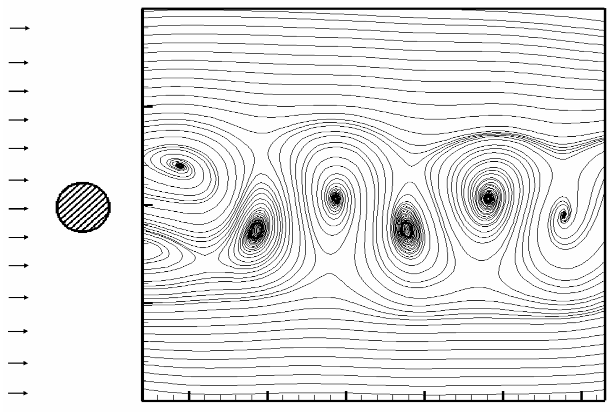

Figure 1.2 Periodic shedding of Karman vortices behind a stationary cylinder.

The dimensionless shedding frequency is expressed by Strouhal number *St* :

$$St = \frac{f_s d}{U} \qquad (1.1)$$

For circular cylinders in laminar flow, *St* ≈0.2. For turbulent flow, the vortex shedding frequency occurs within a frequency band centered at frequency f_s. If the cylinder vibrates in the cross-wind direction at structural natural frequency f_o, the equation (1.1) is also valid as long as shedding frequency f_s is far from f_o. In another occasion, when shedding frequency f_s is close to structural natural frequency f_o, vortex shedding is governed by the cylinder vibration, or Karman vortices shed at the frequency same to cylinder natural frequency, $f_s = f_o$. The synchronization between f_s and f_o is termed as lock-in phenomenon or lock-on *etc.* Within the lock-in wind velocity range, the cable vibration occurs in resonance conditions with large amplitudes because of the in-phase oscillating lift force.

However, Hikami and Shiraishi (1988) argued that the so-called rain-wind-induced cable vibration was not a simple Karman vortex-induced oscillation since the rain-wind-induced vibration was characterized by $f_s >> f_o$. And they also excluded wake galloping mechanism because the cables are separated sufficiently far to avoid any interactions between wakes. Therefore the Karman vortex shedding and lock-in phenomenon, together with the wake galloping, can be excluded from the excitation mechanism.

1.2.2 Den Hartog galloping

For a single degree of freedom system vibrating in cross-wind direction, the instability conditions for Den Hartog galloping can be expressed as:

$$\frac{dC_L}{d\alpha} + C_D < 0 \tag{1.2}$$

where C_L is lift coefficient, C_D is drag coefficient, and α is the angle of wind attack as shown in Figure 1.1 (b).

Smooth circular cylinders usually can not gallop because their symmetric cross-sections result in $\frac{dC_L}{d\alpha} = 0$ and $C_D > 0$ therefore instability criterion (1.2) can not be met. Nevertheless, ice, water rivulet, or other causes of asymmetry, can cause $\frac{dC_L}{d\alpha} < 0$ and produce galloping instability on circular cylinders under certain conditions.

1.2.3 Two-Degree-of-Freedom Galloping

Yamaguchi (1990) alleged that one-degree-of-freedom galloping theory, such as the Den Hartog galloping mentioned in section 1.2.2, was not sufficient to explain the rain-wind-induced cable vibration because the relative position of water rivulets, especially the upper rivulet, circumferentially oscillates on cable surface during each cable vibration cycle. He put forward a two-degree-of-freedom galloping theory which included not only the vertical vibration of a large cylinder and also the circumferentially oscillation around large cylinder axis of a small cylinder acting as the upper rivulet.

Assuming a single mode vibration in vertical *y* direction, the cable equilibrium equation can be written as:

$$m\ddot{y} + ky = F_y \tag{1.3}$$

where m is the cable mass per unit length, k is the stiffness, F_y is the vertical unsteady aerodynamic force acting on the cable per unit length. The rivulet mass is disregarded if compared with the cable mass, and damping ratio is removed in equation (1.3) for simplicity.

The circumferential motion of the rivulet is expressed in terms of inertial force and aerodynamic moment:

$$I\ddot{\theta} = M \tag{1.4}$$

where I is the polar mass moment of inertia per unit length of water rivulet around the cable axis and M is the unsteady aerodynamic moment per unit length.

The unsteady aerodynamic force F_y and moment M can be expressed as:

$$F_y = -\frac{1}{2}\rho U_{rel}^2 (d + D)\{C_D(\alpha)\sin\alpha^* + C_L(\alpha)\cos\alpha^*\} \tag{1.5}$$

$$M = -\frac{1}{2}\rho U_{rel}^2 (d + D) C_M(\alpha) \tag{1.6}$$

where

$$U_{rel} = \frac{U + R\dot{\theta}\cos(\beta + \theta)}{\cos\alpha^*} \tag{1.7}$$

$$\alpha = -\theta + \alpha^* \tag{1.8}$$

$$\alpha^* = \tan\frac{\dot{y} + R\dot{\theta}\sin(\beta + \theta)}{U + R\dot{\theta}\cos(\beta + \theta)} \tag{1.9}$$

With some assumptions, Yamaguchi (1990) conducted eigenvalue analysis and obtained analytical values similar to those acquired from filed observations. His success proved that the two-degree-of-freedom galloping theory is superior than Den Hartog’s one-degree- of-freedom galloping theory in clarifying the mechanism of rain-wind induced cable vibration.

1.2.4 High Speed Vortex Excitation

Matsumoto *et al.* (1998, 2001a) reported that by the visualization with liquid paraffin, secondary vortices were found along cable axis in the near wake of stationary yawed cylinder, and Karman vortex behind a yawed cable could be amplified once every three or four shedding cycles by the interaction between Karman and axial vortices. Therefore the lift force induced by Karman vortex would be intermittently amplified as well. He further hypothesized that if Karman vortex was amplified every fifth or sixth of its shedding frequency, this could well explain the low frequency of rain-wind induced cable vibration. The characteristic frequency of secondary vortices has not been identified yet, but Matsumoto concluded that it was influenced by yaw angle, location of upper water rivulet, end conditions of cylinder, *etc.* Therefore, this possible generation mechanism of rain-wind induced vibration, and the interaction between secondary and Karman vortices in cylinder wake, still deserve further investigation.

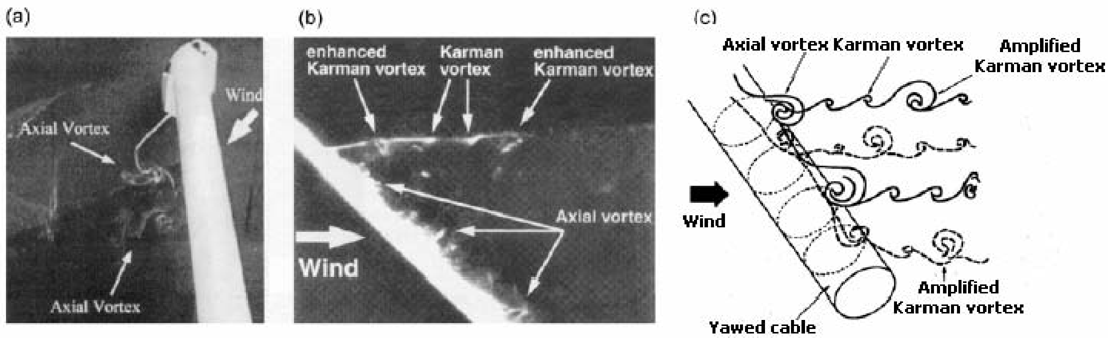

Figure 1.3: (a) paraffin visualization of secondary vortices (or axial vortex) behind cylinder, (b) visualization of secondary vortices and intermittently enhanced Karman vortex, (c) illustration of the interaction between secondary and Karman vortices (Matsumoto *et al.* 2001a).

1.2.5 Countermeasures to suppress rain-wind induced cable vibration

Even though the exact excitation mechanism of rain-wind induced cable vibration has not been identified yet, some empirical countermeasures have been adopted to suppress rain-wind induced cable vibrations due to urgent engineering requests. Dampers and wires connecting cables are commonly used to increase cable damping ratio, and also some surface processing methods such as dimples or spiral wires to spoil the motion and formation of water rivulets. More or less successful as they are, the countermeasures all have some kinds of side effects such as aesthetic (connecting wires and dampers), maintenance (dampers) and aerodynamic cost (surface processing). And the safety and future of cable stayed bridges is still unsure.

For these reasons, the in depth knowledge of the rain-wind induced cable vibration mechanism is still essential for a vibration control technique well balanced among factors of efficiency, cost, maintenance, aesthetics, *etc.*

1.3 Flow structure around a circular cylinder

1.3.1 Primary vortex structure in the wake of a circular cylinder

Whatever the vibration mechanism of rain-wind induced cable vibration is, it is certain that the driven force of the vibration must come from the interactions between cable and the flow field surrounding it. Neither the verification of above mentioned mechanisms nor the establishment of a new one can stand without an accurate physical interpretation of the surrounding flow filed. In sharp contrast to the wealth of reports that are concerned with the relationship between cable vibration behaviors, *e.g.* amplitudes and frequencies, and the properties of incoming flow, *e.g.* velocities, turbulent intensities and attacking angles, there are few reports investigating wind forces acting on cable in a case of rain-wind induced vibration, and even fewer trying to deduce the acting wind forces from the flow field surrounding the cable. Therefore the main objective of present work is to investigate fluid-structure interactions by linking the wind forces with flow fields.

To an ideal cylinder, which is a circular cylinder of infinite length with smooth surface and symmetrical cross-section placed perpendicular to flow, the flow field around it has attracted interests from researchers and engineers for almost one century, because this phenomenon has not only many interesting fundamental properties but also great practical importance. Although real rain-wind induced cable vibrations mostly occur when cables with asymmetrical cross-sections (Figure 1.1b) are inclined to wind, it is still very necessary to start our physical interpretation from the basic fluid dynamics around the ideal circular cylinders due to the complexity of inclined cases.

When a flow moves around a stationary cylinder, a region of disturbed flow is always formed around and behind the cylinder. The properties of the disturbed flow, and the fluid actions that feed back from the flow to the cylinder, mainly depend on the relative velocity between the two objects, though many other factors such as turbulence, surface roughness, cylinder length *etc.* can also have some influences. For a fluid-cylinder system with given physical properties, the relative velocity can be represented by Reynolds number *Re* ($Re \equiv \frac{U_\infty d}{\nu}$, where U_∞ is the free-stream velocity, d is the characteristic height of the cylinder and ν is the kinematic viscosity of fluid). Zdravkovich (1997) suggested following four regions that construct the disturbed flow field:

(i) one narrow region of retarded flow, usually termed as stagnation region even though the flow inside is not really stagnant;

(ii) two boundary layers attached to the surface of the cylinder;

(iii) two sidewise regions of displaced and accelerated flow;

(iv) one downstream region of separated flow called the wake.

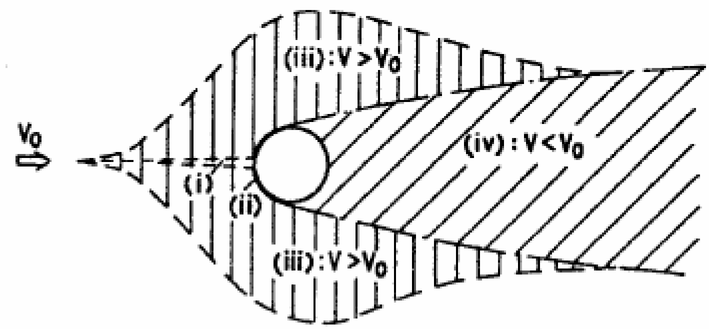

Figure 1.4: Regions of disturbed flow. (Zdravkovich 1997)

Inside the region of wake, the most prominent periodic phenomenon is the alternative shedding of Karman vortices from two cylinder sides. Reynolds number has considerable influence on the characteristics of vortex shedding wake. The wake regimes generated at different Reynolds numbers can be divided as following:

a) Creeping flow regime: at very low Reynolds numbers (*Re* < 5) the flow is entirely laminar and keeps attached to the cylinder surface.

b) Steady separation regime: 5 < *Re* < 40. Flow separation begins to occur at the rear of the cylinder and form a pair of attached eddies. With increasing *Re*, the separation points move upstream.

c) Periodic laminar regime: 40 < *Re* < 180. Above Reynolds number of about 40 the instability of the shear layers begins the development of a vortex street with vortices being shed alternately from either side of the cylinder. The periodic shedding frequency rises with increasing *Re*.

d) Transition in shear layer or sub-critical regime: 180 < *Re* < $2-3\times10^5$. In this regime, vortex shedding becomes irregular. Separation point of laminar boundary layer on cylinder surface moves forward with increasing *Re*. When *Re* value reaches the order of 10^5, separation point occurs on the forward side of the cylinder at a angle between 70° and 80° from stagnation point. It should be noted that for filed observations of rain-wind induced cable vibration, their occurrence *Re* values are just around the order of 10^5, and upper water rivulet flows on cable surface between angular positions 40° and 70°, which may lead to early boundary layer separation. The effect of this alternation on flow field has not been experimentally studied yet.

e) Transition in boundary layer or critical regime: $2-3\times10^5$ < *Re* < 7×10^5. In this regime, the laminar boundary layer separates initially between 90° to 100° from stagnation point, closely in front of the transition point to turbulent flow. Because the turbulent boundary layer can withstand a greater adverse pressure gradient, the boundary layer will reattach to surface between 120° to 140°, and enclose a separation bubble. This re-attachment phenomenon results in a higher base pressure and cause a rapid drop in the value of drag coefficient.

f) Super-critical regime: $7\times10^5 <$ *Re* $< 3.5\times10^6$. In this regime, the transition point occurs before the separation point and flow separation takes place only once. Consequently the separation bubble disappears.

1.3.2 Secondary vortex structure in the wake of a circular cylinder

In addition to the prominent and intensively investigated Karman vortex structure, there is another less studied vortex structure in cylinder wake, secondary vortices which appear when *Re* > 150 and undertake a transition around *Re* = 240.

Due to the difficulties in quantitative measurements of the secondary vortices, up to now qualitative information, such as generated by flow visualization, still occupies considerable portion of our knowledge about them. And for same reason the few conducted quantitative investigations mostly concentrate in low *Re* range. As mentioned in section 1.2.4, Matsumoto *et al.* (1998, 2001a) found with qualitative measurements that in high *Re* range there may exist strong interaction between Karman and secondary vortices, and he further speculated that their resonance frequency may provide a possible explanation to the excitation of rain-wind-induced cable vibration. Mutsumoto's speculation induced our starting research step: to investigate the three-dimensional wake structures, including both Karman and secondary vortices, in relative high *Re* range with quantitative measurements.

1.4 Motivation and Objectives

Previous work has greatly improved our understanding of the rain-wind-induced cable vibration. However, past reports in the literature are not always consistent with each other. For example, while many observations of the rain-wind-induced vibration were made at a yaw angle (mostly near 45°), Verwiebe & Ruscheweyh (1998) reported the damage of nearly vertical steel bars of a new bridge due to the same vibration. Flamand (1995) conducted full-scale wind tunnel tests and observed the rain-wind-induced cable vibration. Once replacing the moving rivulets by false fixed rivulets glued on the cable surface, he could not observe the vibration again. He concluded that the oscillation of the upper water rivulet played a crucial role for the generation of the rain-wind-induced vibration. The same opinion was shared by Verwiebe & Ruscheweyh. The latter authors further interpreted that the oscillation of water rivulets resulted in a variation in the cable cross-section shape and hence in the pressure distribution around the cable. Consequently, the resultant force on the cable was varying and exciting the cable. On the other hand, Bosdogianni & Olivari (1996) used two bars of various shapes to simulate the water rivulets and observed a strong increase in the oscillation amplitude of the cable. Therefore, they contested that it was the protuberances at certain positions on the cable surface that caused the rain-wind-induced vibration, and the oscillation of water rivulets or the shape of the simulated rivulets had little or no influence on the instability. Matsumoto *et al.* (1995) advocated three types of the rain-wind-induced cable vibration, namely, the “galloping” type, the vortex-shedding type and a combination of both. The vortex-shedding type was characterized by a period longer than the classical Karman vortex shedding. The galloping type included both divergent galloping and velocity-restricted galloping. They further linked the velocity-restricted galloping to the three dimensionality of the Karman vortex. Based on the power spectrum of the lift force and flow visualization, Matsumoto *et al.* (1998, 2001a) proposed that the fluid interaction between Karman and axial vortices could be responsible for the rain-wind-induced cable vibration.

Accumulated understanding has guided the development of a number of techniques in bridge engineering to alleviate the problem, for example, increasing damping by using damping ropes between the cables, dynamic vibration absorbers, and dashpots at the cable footing, deflecting water on the cable surface or preventing the water rivulets from oscillating circumferentially. However, these techniques are far from adequate, probably because many aspects of the rain-wind-induced vibration have yet to be clarified, including its generation mechanism. Existing investigations mostly focused on engineering issues such as how, when and where the problem occurs and how to prevent the problem from occurring; there does not seem to have a systematic research on the fundamental aspects of this important engineering problem, especially on fluid dynamics associated with this problem in spite of the fact that the rain-wind-induced vibration originates from the fluid excitation force. There has been a wealth of papers in the literature in regarding to the wake of a yawed stationary or oscillating cylinder. It is the flow behind the yawed cylinder (both stationary and oscillating) with running water rivulets that needs more attention. Matsumoto *et al.* (1998, 2001a) have identified the importance of axial flow/vortices in the generation of the rain-wind-induced vibration. But the axial flow/vortex mechanism is not entirely clear. A number of other issues can be also crucial to understand thoroughly this problem. How does the occurrence of water rivulets affect the near-wake fluid dynamics of the cable, including the vortex formation process, dominant shedding frequency, flow structure and downstream evolution? How do the water rivulets and their oscillation change the coupling between fluid dynamics and structural dynamics? These issues warrant an in-depth investigation on fluid dynamics, structural dynamics and their non-linear coupling and motivate present study.

1.5 Thesis outline

The present work aims to investigate fluid-cylinder interactions, especially the wake structure behind a cylinder with and without the presence of water rivulets.

In chapter 1, the background of present project and related previous literature are introduced and reviewed, and the motivation and outline of this investigation are presented.

In chapter 2, experimental facilities and details including applied instruments and their measurement principles are introduced.

In chapter 3, three-dimensional wake structure behind a fixed smooth cylinder at relatively high *Re* range was experimentally and quantitatively investigated by Particle Imaging Velocimetry. Characteristics of three-dimensional vortex structures are presented and compared.

In chapter 4, wake structure behind an inclined smooth cylinder with or without running water rivulets was experimentally investigated by Particle Imaging Velocimetry and Laser Doppler Anemometer. It was found that inclination angle of cylinder has important effect on vortex strength.

In chapter 5, conclusions and future recommendations based on present work are summarized.

Chapter 2: Experimental Facilities and Details

2.1 Overview

Due to the complexity of aerodynamic related phenomena, solutions to most of wind engineering problems heavily rely on the investigations conducted in wind tunnels to provide reliable database. The thriving numerical methodologies, such as Computational Fluid Dynamics, offer good possibility to solve aerodynamic problems. However, by far popular numerical methodologies are far from solving questions in critical *Re* range where rain-wind induced vibration occurs. Furthermore, the interaction between wind and structure will be even more complicated than pure aerodynamic questions, especially when the induced structural displacements are large enough to significantly modify the boundary conditions of the flow itself. In this case, the simultaneous solution of the Navier-Stokes equations for the flow and of the elastic or non-elastic structural modeling equations is required, which is far beyond the capability of today's numerical methodologies. Therefore simplified theoretical modeling and wind tunnel investigations are commonly used for practical purpose.

For investigations conducted in wind tunnels, flow blockage is one of precautions for relatively large models if placed in wind tunnels of limited size. For cylinders, the blockage is defined as the ratio of diameter d of the model to the height H of the test section, $B = \frac{d}{H}$. Blockage ratios less than 7% are usually acceptable, otherwise the pressure distribution on cylinder surface will be severely distorted to alter flow pattern.

2.2 Setup for the measurement of fluid dynamics around a cylinder without running water rivulets

2.2.1 Experimental Setup of model and measurement instrument

Experiments were conducted in a closed cycle wind tunnel with a test section in the size of 600 (*H*) x 600 (*W*) x 2000 (*L*) mm. Velocity range is 0.5 – 50 m/s and most stable around 7 m/s, with a background turbulence <0.5%. A cylinder of diameter d = 12.7 mm and effective length L = 600 mm was used to generate the wake. Free stream velocities, U_∞, were set to 2.4 m/s, 6 m/s, and 12 m/s to result in Re = 2000, 5000 and 10000.

A set of Particle Imaging Velocimetry (PIV), Dantec PIV2100 system, was utilized for velocity and vortex measurement in the wake. Wind flow was seeded by paraffin oil particles whose mean diameter is around 1 μm. The seeded flow was illuminated by two identical Nd:YAG pulsed lasers. Each laser pulse is of 120 mJ energy and lasts 8 ns to freeze the flow pattern at the flashing moment. A Hisense double image CCD camera with 1280 x 1024 pixel resolution was used to capture images of the illuminated flow. Velocity vectors were extracted from images by 32 x 32 pixel 50% overlap cross-correlation, corresponding to 1.9 mm spatial resolution, or 0.15 d. As target vortices have a diameter around 1 d, each of vortices will be illustrated by about 6 x 6 = 36 velocity vectors.

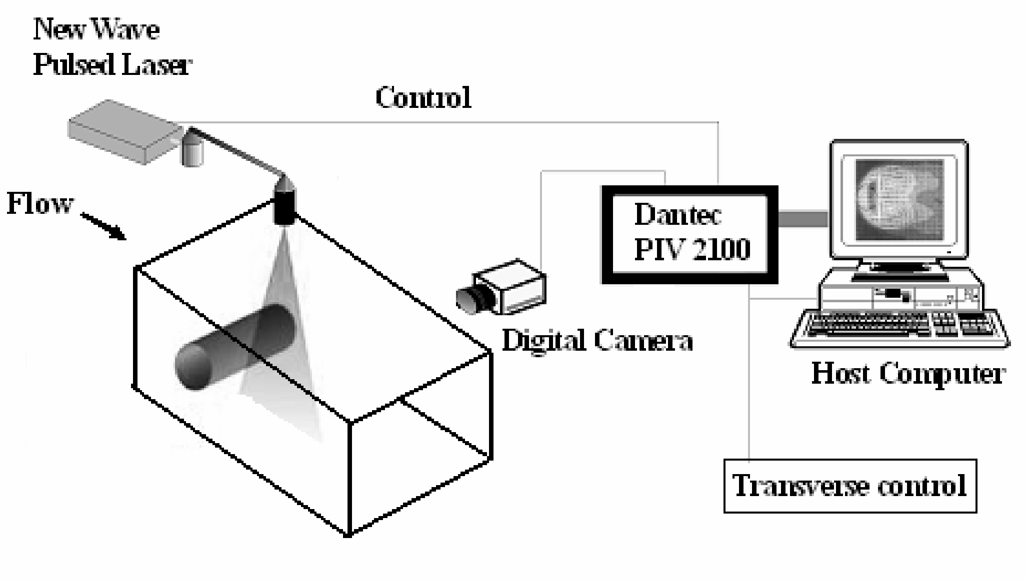

Figure 2.1: Typical experimental setup of PIV and test model in wind tunnel.

2.2.2 Principle of Particle Imaging Velocimetry

In PIV, the velocity vectors are derived from sub-sections of the target area of the particle-seeded flow by measuring the displacement of moving particles between two consecutive light pulses: $V = \frac{\Delta X}{\Delta t}$.

First, target flow is filled with seeding particles, whose mean diameter is around 1 μm for applications in air, at a concentration of around 0.1%. Then the flow is illuminated twice with preset time interval Δt in the target area by light sheets. The CCD camera is able to capture each light pulse in separate image frames. Once a sequence of two light pulses is recorded, the images are divided into small subsections called interrogation areas. The interrogation areas from each image frame, I1 and I2, are cross-correlated with each other, pixel by pixel. The correlation produces a signal peak, identifying the common particle displacement,

ΔX . An accurate measure of the displacement, and thus also the velocity, is achieved with sub-pixel interpolation.

A velocity vector map over the whole target area is obtained by repeating the cross-correlation for each interrogation area over the two image frames captured by the CCD camera.

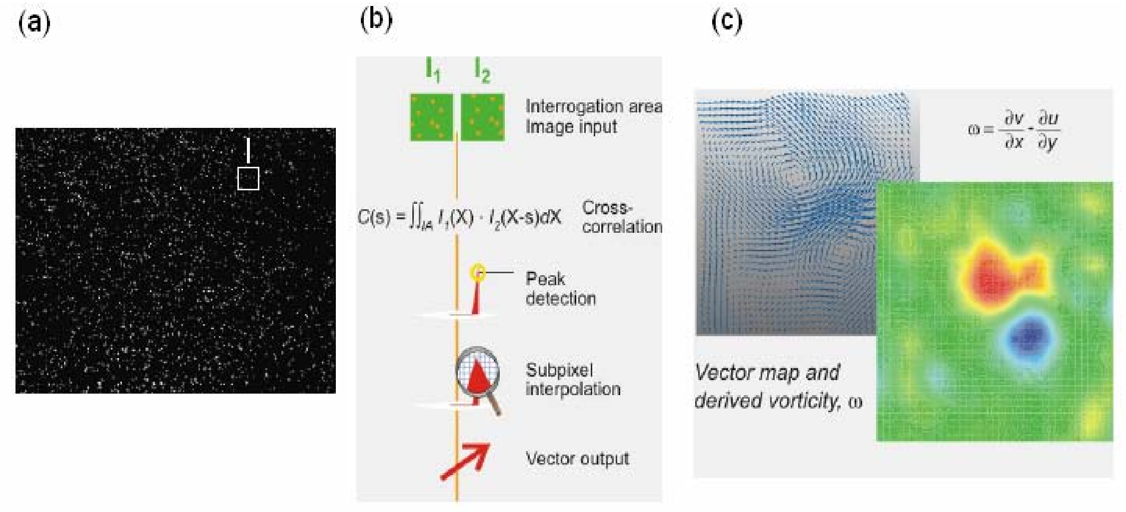

Figure 2.2: (a) One of the two captured images for the seeding particles in flow. A random interrogation area in frame, I, is marked out; (b) data processing procedures to extract vector from particle images within same interrogation area I; (c) vector map and derived vorticity map (courtesy of Dantec Dynamics A/S).

Particle Image Velocimetry is a non-intrusive and whole-flow-field diagnostic technique providing 2D instantaneous velocity vector measurements in the cross-section of a flow, which is suitable for present study of vortex structure.

2.3 Setup for the measurement of fluid dynamics around an inclined cylinder with running water rivulets

2.3.1 Experimental setup of model and measurement instrument

Same wind tunnel as that in section 2.2.1 was used. Cylinders of diameter *d* = 19 or 45 mm and effective length *L* = 600 mm was used to generate the wake. Free stream velocities U_∞ were set within range 6 m/s – 16 m/s to simulate real wind flow.

In addition to PIV, a set of 2D Laser Doppler Anemometer (LDA), Dantec 58N40, is utilized. A LDA probe equipped with a front lens of 400 mm focus length is used to acquire time averaged flow velocities around cylinder. Four laser beams of two colors, *i.e.* green (wavelength 514 nm) and blue (488 nm), are transmitted from the LDA probe and focused at 400mm in front of the probe. Their intersection volume, which is also called measurement volume, is an ellipsoid with 1.18 mm minor axis and 2.48 mm major axis. The flow was also seeded by paraffin oil particles whose mean diameter is around 1 μm. Velocities of particles passing through the measurement volume will be recorded in sequence by the LDA. Typical sampling rate is usually between 1000-2000 Hz, which is adequate for the max. 100 Hz Karman vortex shedding frequency.

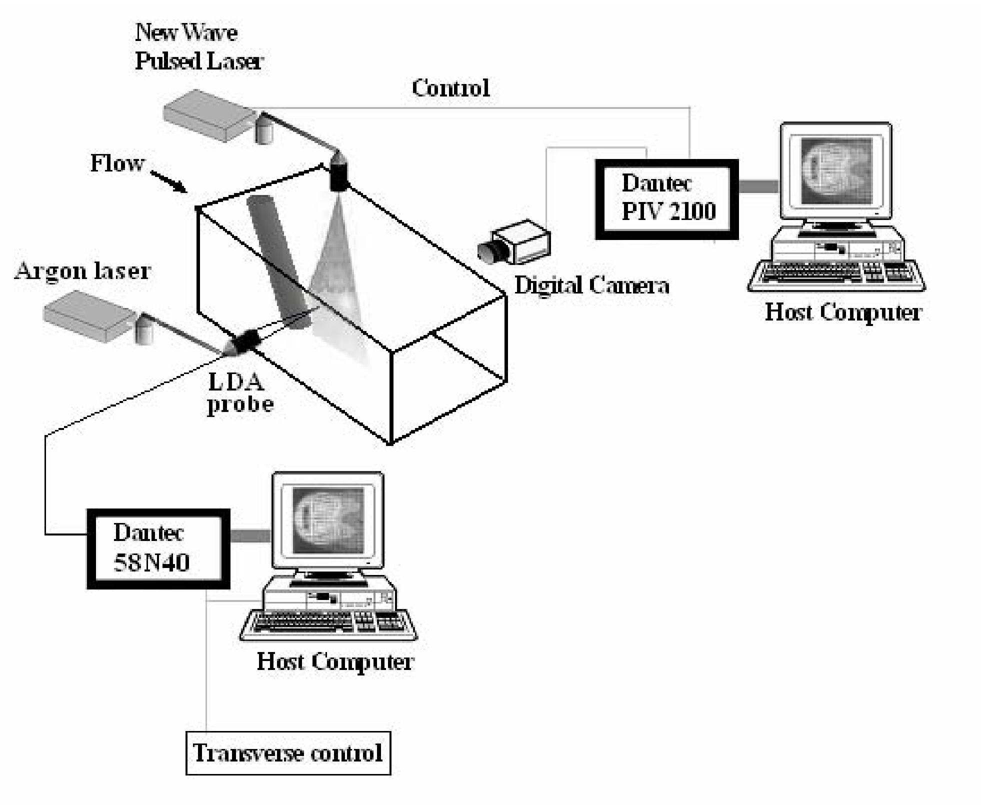

Figure 2.3: Typical experimental setup of PIV, LDA and test model in wind tunnel.

2.3.2 Principle of Laser Doppler Anemometer

The LDA, is a widely accepted tool for fluid dynamic investigations in gases and liquids and has been used for more than three decades. It is a well-established technique that gives information about flow velocities.

In LDA probe, parallel exit laser beams from fibers are focused by a front lens to intersect in a measurement volume. The light intensity inside the volume is modulated due to interference between the laser beams. The interference produces parallel planes of high light intensity, so called fringes. The fringe distance d_f is defined by the wavelength λ of the laser light and the angle θ between the beams: $d_f = \frac{\lambda}{2\sin(\frac{\theta}{2})}$. d_f is a constant for each set of manufactured LDA.

Every seeding particle passing through the measurement volume scatters light proportional to its local light intensity. The scattered light is collected by probe front lens and focused on a photo-detector. An interference filter, mounted between the lens and the photo-detector, only allows required wavelength to pass to the photo-detector. The filter is used to remove noise from ambient light and from other wavelengths. Photo-detector converts the fluctuating light intensity to an electrical signal, which is filtered and amplified to determine transient time t_f for each particle in the LDA signal processor 58N40. Velocity can be calculated by: $V = \frac{d_f}{t_f}$.

LDA is a kind of non-intrusive point measurement technique with high spatial and temporal resolution, therefore is chosen in present experiment to investigate time averaged flow velocities.

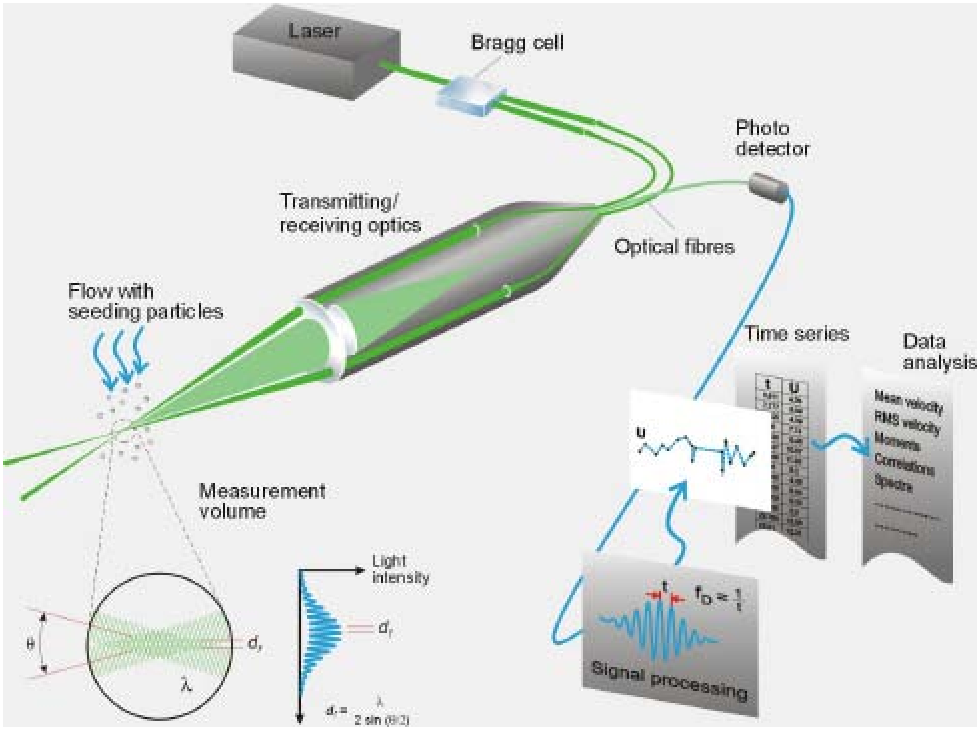

Figure 2.4: Illustration of LDA measurement principle. (courtesy of Dantec Dynamics A/S)

Chapter 3: Three-dimensional wake structure behind a circular cylinder in the absence of water rivulets

3.1 Introduction

As previously mentioned in Section 1.2.4, the three dimensional cylinder wake, including Karman vortices (or named as spanwise vortices) and axial vortices (or named as transverse or streamwise vortices dependent on investigation planes), is one of the interesting directions that may provide explanation to the exciting mechanism of rain-wind induced cable vibration. It is necessary to start from the three dimensional wake of a smooth cylinder without water rivulets for its simplicity, and then extend to cylinder with water rivulets, which will be described in Chapter 4.

The three dimensionality of a plane cylinder wake has been given a significant attention in literature. Hama (1957) by means of flow visualization noted that vortex structure behind a two-dimensional (2D) cylinder turned to be three-dimensional (3D) at *Re* > 150 ($\equiv \frac{U_\infty d}{\nu}$, where U_∞ is the free-stream velocity, d is the characteristic height of the cylinder and ν is the kinematic viscosity of fluid). That was perhaps the first report for the existence of streamwise vortices. Later a number of insightful reports were generated from other flow visualization experiments. For example, Gerrard (1978) observed some regular appearance of 'knots' and 'fingers' within *Re* range 140 ~ 500, which were footprints of the so-called secondary vortices. Based on their flow visualization results in a circular-cylinder near wake in *Re* range 1.2 x 10^3 ~ 1.1 x 10^4, Wei & Smith (1986) found that the secondary vortices underwent a three-dimensional distortion immediately following their formation behind the separation point. They speculated that the distortion was the origin of counter-rotating streamwise vortices. Bernal & Roshko (1986) studied mixing layers behind a plate based on laser-induced fluorescence flow visualization at *Re* = 1900 ~ 3000 and found that the wavelength of secondary vortices is almost two third as long as that of Karman vortex. Williamson (1988) detected that there exist two types of secondary vortices, i.e., mode A that occurs at *Re* = 160 ~ 240 with a wavelength of about 3*d*, and mode B that occurs at *Re* > 240 with a wavelength of about 1*d*. By hydrogen bubble flow visualization, Muchmore & Ahmed (1993) reconfirmed Williamson's finding within extended *Re* range from 330 to 2.1 x 10^4 and further noticed that streamwise vortices significantly distorted the upstream side of Karman vortices. Mansy *et al*. (1994) applied a scanning laser anemometer (SLA) to measure a cylinder wake and detected that streamwise vortices occur at random spanwise locations. At same *Re* number, the wavelength of streamwise vortices increases with *x/d* until reaching 1.3 ~ 1.4*d* at *x/d* = 15 ~ 30. On the other hand, at same *x/d* location the wavelength-*Re* relationship was found to be $Re^{-0.5}$.

Flow visualization is excellent in providing qualitative information on a flow, but cannot offer quantitative data and sometimes can be even misleading because of the possible decoupling between markers and flow. Hot-wire technique has been long and frequently utilized to provide quantitative data of the cylinder wake; for example, Zhou & Antonia (1994a) used 16 X-wires, aligned in two orthogonal planes, to detect the three dimensional vortical structures in a turbulent cylinder wake. However, hot-wire technique is intrusive and suffers from measuring only a very limited number of points in the flow field. In 1990s Particle Image Velocimetry (PIV) technique became mature, which could capture instantaneous 2D flow fields, providing both qualitative and quantitative information of the flow. The PIV led to a surge of studies on the three dimensionality of cylinder wake. Using this technique, Wu *et al*. (1994b) measured longitudinal and spanwise vortices at Re = 525 in a circular-cylinder near wake and found that $\omega_{y,\max} \approx 1.6\omega_{z,\max}$ and $\Gamma_y \approx 0.11\Gamma_z$, where $\omega_{y,\max}$ and $\omega_{z,\max}$ were the maximum lateral and spanwise vorticities, respectively, and Γ_y and Γ_z were circulations associated with the two types of structures. Lin *et al.* (1995a) applied PIV at x/d = 1 and $Re = 10^4$ to measure streamwise vortices and observed that the spanwise wavelength of these vortices was around 1d, and the averaged circulation was one tenth of Karman vortices. Brede *et al.* (1996) measured the circulation and wavelength of streamwise vortices for both mode A (at x/d = 6 and Re = 160 ~ 240) and mode B (at x/d = 2 and Re = 240 ~ 500).

For conventional PIV technique, two light sheets overlap in space and a camera may capture the same group of seeding particles given a sufficiently small time interval between two consecutive images. Then the velocity information can be extracted from the cross-correlation between particle locations recorded in the two images. This arrangement has proved to be successful for PIV measurements in the (x, y)- and (x, z)-planes (coordinate system is defined in Figure 3.1), where the particle motion is on average in-plane. For the measurement of the streamwise vorticity in the (y, z)-plane, however, it may not work so well because all particles have a large streamwise velocity component out of sampling plane therefore it is difficult for two light sheets separated in time to capture the same group of seeding particles, which results in a poor cross-correlation result between particle locations on two consecutive images. The situation can become worse at a high *Re* or downstream of the vortex formation region, where the mean streamwise velocity component increases significantly, compared with that in the immediate proximity to the cylinder. This is probably why the PIV reports for the (y, z)-plane are scarce, relatively to those for the (x, y)- and (x, z)-planes, mostly being obtained either in the region of $x/d \leq 2.5$ (*e.g.* at $x/d \leq 2.5$ by Lin *et al.* 1995a and Chyu & Rockwell 1996 for $Re = 10^4$) or at relative low *Re* (*e.g.* up to $x/d = 10$ at $Re < 500$ by Brede *et al.* 1996), where the out-of-plane velocity component is small. Therefore, the first objective of present research is to develop a modified PIV technique that has an improved capability to measure reliably the streamwise vorticity at a relatively large x/d and *Re*. In the view of the fact that most of the longitudinal structure data were obtained in a close proximity to the cylinder, our second objective is to measure and investigate the longitudinal structures further downstream, in particular, at a relatively high *Re* range, thus complementing the data in the literature.

3.2 EXPERIMENTAL DETAILS

Experiments were conducted in a closed circuit wind tunnel. Working section is of 0.6 m × 0.6 m and 2 m long with windows made of optical glass to maximize the signal-to-noise ratio for camera imaging. A copper tube of diameter d = 12.7 mm was horizontally mounted across the center of working section, resulting in an aspect radio of 47. Experiments were carried out at free stream velocities U_∞ = 2.4, 6.0 and 12.0 m/s, the corresponding Reynolds number Re ($\equiv U_\infty d / \nu$) = 2000, 5000 and 10000, respectively. The background longitudinal turbulence intensity is approximately 0.4%. Experimental arrangements and measurement planes are schematically shown in Figure 3.1. The origin of the coordinate system is defined at the center point of the cylinder, with x, y and z directed along the streamwise, transverse and spanwise directions, respectively.

A PIV2100 system made by Dantec was used to measure the flow, which was seeded by smoke, generated from Paraffin oil, with the averaged particle size of around 1 μm in diameter. A Newwave double-cavity pulsed laser (each cavity having a maximum energy output of 120 mJ at 532 nm wavelength) and a mirror-lens system were used to produce a 1-mm-thick light sheet. A Hisense CCD camera (double-frame, 1280×1024 pixels, 12-bit, 4-pair/second) was used to capture flow images. Camera acquisition and laser illumination was synchronization by Dantec PIV2100 processor. The camera captured an area of x/d = 0.8 ~ 12.5 and y/d = -4 ~ 4 for the flow in (x, y)-plane and an area of x/d = 0.5 ~ 12 and z/d = -4 ~ 4 for the flow in (x, z)-plane. The measurements in (x, z)-plane were conducted at $y/d = 0$ and 0.5. Measurements in (y, z)-plane covered an area of $y/d = -4 \sim 4$ and $z/d = -5 \sim 5$ and were performed at $x/d = 5$, 7, 10, 15 and 20. A total of 200 PIV images were obtained for each measurement plane.

To overcome the difficulty caused by large out-of-plane velocity component for the (y, z)-plane measurement, light sheet 2 was spatially displaced downstream, relative to light sheet 1, so that it could capture the same group of moving seeding particles that had already been captured by light sheet 1, as schematically illustrated in Figure 3.2. The displacement, δ, was adjusted by trial and error until the success ratio of cross-correlation reached a level as good as that for (x, y)- and (x, z)-planes (typically $\geq 95\%$).

The captured raw digital particle images were fed to Dantec Flowmanager software for analyzing. The velocity vectors were generated by 32×32 pixels with 50% overlap FFT cross-correlation. An array of 79 x 63 or a total of 4977 vectors was generated for each pair of images. Uncertainty of the velocity generation was verified by a pair of artificially doted images. All dots in the first image were shifted right by 10 pixels in second one, corresponding to an ideally 7.830m/s rightward velocity component. In comparison with PIV's real analysis result 7.825m/s, uncertainty of velocity was < 1%. The same number of vorticity data was derived based on the velocity vectors, with a spatial resolution of 1.7 mm or 0.14 d. It should be noted, however, that the Kolmogrov length scales of the present wake are 0.17 mm, 0.12 mm and 0.076 mm at $x/d = 10$ for $Re = 2500$, 5000 and 10,000, respectively. See Yiu *et al.* (2004) for the estimate of the scales, where the wake generated by a cylinder of the same diameter was measured at similar Reynolds numbers. On the other hand, the spatial resolution of the present vorticity estimate based on PIV images was 1.7 mm or 0.14d in the three measured planes. The degradation of the spatial resolution of vorticity worsens for higher Reynolds numbers and for ω_x and ω_y structures, which have smaller scales. The readers are cautioned that the quantitative comparison between ω_x, ω_y and ω_z in this paper is only indicative, not conclusive. Nonetheless, this smoothing effect should not have a great impact on the present investigation, which focuses on the vortical structures, not on the documentation of the three vorticity components.

3.3 SPANWISE VORTICES

The iso-contours of spanwise vorticity, $\omega_z^* = \dfrac{\omega_z d}{U_\infty}$, are presented in Figure 3.3. They display the well known Karman vortex street. In this part, the asterisk denotes normalization by U_∞ and/or d. The cut-off level of ω_z^* is 10% of the maximum vorticity ($\omega_{z,\max}^*$). For the ease of comparison, cut-off level and contour increment are same for the three different Reynolds numbers. To quantify the size of vortical structures, d_x^* and d_y^* are used to denote the streamwise and the lateral extents, respectively, of a spanwise vortex. Figure 3.4 presents the averaged vortex size, $\overline{d}_x^*$ and $\overline{d}_y^*$. Unless otherwise stated, overbar denotes in this paper an averaged quantity obtained from 200 PIV images. In the near wake of the cylinder

($3 < x^* < 4.6$), the vortex size, in particular, d_x^* grows rapidly because of the vortex formation process. At $x^* \approx 4.5$, d_x^* and d_y^* have almost equal values, about 2.74, regardless of *Re*, suggesting that the shape of spanwise vortices turns approximate round here. This size is in agreement with Cantwell & Coles' report (1983, later referred to as CC in this paper) that the vortex diameter at $x^* = 6.47$ was 2.68 *d* (*Re* = 1.4 x 10^5, the cutoff level = $0.1\,\omega_{z,\max}^*$), which was reduced from their vortex area. Further downstream d_x^* and d_y^* expand at slow rate. The vortex formation length is in general defined as the distance between the cylinder centre and the location where the maximum streamwise fluctuating velocity occurs (Bloor 1964). Since the data of this maximum fluctuating velocity is presently unavailable, we give an alternative definition of the vortex formation length as the distance from the cylinder centre to the position where the vortex reaches its full size, *i.e.* 2.74 *d*. The formation length based on the data presented in Figure 3.4 is 4.5 *d* at *Re* = 2000, 4.4 *d* at *Re* = 5000 and 4.2 *d* at *Re* = 10000. This result is consistent with previous reports that the vortex formation length reduces with *Re*.

The vortex center is often defined as either the highest concentration of spanwise vorticity (e.g. Hussain & Hayakawa 1987; Zhou & Antonia 1993) or the centroid of an effective vortical structure (CC). The latter definition is chosen for this work, therefore the position of a vortex centroid is determined by

$$x_c = \frac{1}{\Gamma_z}\int_A x\omega_z\, dA, \qquad \text{(3-1)}$$

$$y_c = \frac{1}{\Gamma_z}\int_A y\omega_z dA. \qquad (3\text{-}2)$$

In the above equations, Γ_z is the circulation associated with the spanwise vortex. In this paper, the circulation associated with vortical structures is estimated by

$$\Gamma_i = \int_A \omega_i dA, \qquad (i = x, y, z) \qquad (3\text{-}3)$$

where A is the effective area of a spanwise, transverse or streamwise vortical structure, determined by a cutoff level = 10% of the peak vorticity.

The averaged streamwise and lateral velocity components at the vortex centroid are considered as convection velocity components $\overline{U}_c^*$ and $\overline{V}_c^*$ of the spanwise vortex. The estimation of $\overline{U}_c^*$ presented in Figure 3.5a is in general agreeable with other reports (e.g. CC, Hussain & Hayakawa 1987; Zhou & Antonia 1993). Apparently, $\overline{U}_c^*$ is not very sensitive to *Re*. $\overline{U}_c^*$ increases steadily from about 0.65 at x^* = 3 to near 0.8 at x^* = 6. In comparison, CC's measurement reached 0.8 at $x^* \approx 4.5$, probably because of their much higher *Re*, hence the shorter vortex formation length. $\overline{V}_c^*$ (Figure 3.5b), determined based on the upper row vortices of negative ω_z^* (above the centerline), is in reasonable agreement with CC's result; it reaches about - 0.14 at x^* = 3, apparently due to the motion of shedding vortices, and then drops rapidly in magnitude till x^* = 5, where the vortex formation is complete. At x^* = 5 - 9, $\overline{V}_c^*$ appears fluctuating about the zero. For x^* > 9, the value of $\overline{V}_c^*$ is almost negligible.

Figure 3.6 presents the trajectory of spanwise vortices given by the variation of the averaged vortex centroid location, $\overline{y_c}^*$, with x^*. Agreement between this trajectory at Re = 10^4 and CC's data is reasonable, but not so good at Re = 2 x 10^3 and 5 x 10^3, probably due to the Re effect. Note that $\overline{y_c}^*$ displays an oscillating path for x^* < 8, internally consistent with the variation in $\overline{V}_c^*$. This oscillating motion was previously observed but not discussed by CC. The vortex, immediately after shedding, is 'pulled' towards or across the centerline under the low base pressure, and then is pushed out towards the free-stream because of the following opposite-signed vortex growth, leading to increasing $\overline{y_c}^*$ from $x^* \approx 3$ to 4.5. This vortex moves towards the centerline again from $x^* \approx 4.5$ to 5.5 ~ 6.5, probably under the rolling up influence of the following vortex of the same sign. This oscillating motion is repeated until $x^* \approx 8$, albeit in a smaller scale with increasing x^*. The $\overline{y_c}^*$ value approaches a constant, 0.36, at $x^* \approx 8$ and, if extrapolated, agrees with Hussain & Hayakawa's (1987) and Zhou & Antonia's observations at x^* = 10.

The streamwise evolution in the strength of vortices can be described by the variation of $\overline{\omega}^*_{z,\max}$ and $\overline{\Gamma}^*_z$ associated with the spanwise vortex, as shown in Figure 3.7. The measured $\overline{\omega}^*_{z,\max}$ changes little with Re, and decays with x^* (Figure 3.7a). The present measurement of $\overline{\omega}^*_{z,\max}$ agrees well with CC's data up to x^* = 5, but appreciably greater for x^* > 5. CC's data was a conditional average based on a pressure signal measured by a pitran sensor on the surface of the circular cylinder 65° away from the forward stagnation point. When the data are acquired at a place far away from where the conditioning signal is sampled, a significant jitter in the vortex location may occur, especially in a highly turbulent flow. As a result, the averaged maximum vorticity may be smeared and thus considerably reduced. Interestingly, $\overline{\omega}^*_{z,\max}$ displays two distinct sections of decay, following the empirical relationship $\overline{\omega}^*_{z,\max}$ = 3.1 - x^* /3 up to x^* = 4.5 and $\overline{\omega}^*_{z,\max}$ = 1.87 - x^* /19 for x^* = 4.5 ~ 11. As mentioned earlier that $\overline{y_c}^*$ increases rather rapidly up to x^* = 4.5 probably because of the ‘push’ by the following opposite-signed vortex, which is in the process of shedding and rapidly growing. It may be inferred that this rapid decay is probably the results of the vigorous interaction between two successive vortices of opposite sign, more specifically, the cancellation between positive and negative vorticity associated with the two vortices, respectively. The observation may be further connected to the variation of the vortex size, which reaches the full size at x^* = 4.5. The coincidence of the three events, all at x^* = 4.5, may suggest that the alternative definition of the vortex formation length based on the growth of the vortex size is sensible. Beyond x^* = 4.5 or the vortex formation region, the decay in $\overline{\omega}^*_{z,\max}$ slows down since the interactions between neighboring vortices are less vigorous, as a result of increased spacing both longitudinally and laterally, than within the vortex formation region.

In Figure 3.7b the measured $\overline{\Gamma}_z^*$ agrees quite well with CC's data even beyond $x^* = 5$. While the averaged maximum vorticity is significantly sensitive to the jitter in the detection of vortex locations, the circulation is an integrated quantity over the whole vortex area and thus less sensitive to the jitter. The variation in $\overline{\Gamma}_z^*$ is different from that in $\overline{\omega}_{z,\max}^*$, first rising up to $x^* \approx 3.5$ due to the growing vortex size and then descending because of the interactions between adjacent vortices. A relatively fast decay from $x^* \approx 3.5 \sim 4$ to 4.5 is still evident. Note that both $\overline{\omega}_{z,\max}^*$ and $\overline{\Gamma}_z^*$ tend to be smaller for higher *Re*. This is probably because of the higher *Re*, the more vigorous the interactions between adjacent vortices.

3.4 Transverse Structures

The iso-contours of transverse vorticity, ω_y^*, measured in the (*x*, *z*)-plane at $y^* = 0.5$ are presented in Figure 3.8 (a), (b) and (c). The cut-off level ($|\omega_y^*| = 0.20$) of the ω_y^* contours is again 10% of the maximum vorticity, $\omega_{y,\max}^*$. For comparison purpose, cut-off level and contour increment are same for the three different Reynolds numbers. In the near wake of the cylinder, the transverse vortical structures occur alternately in sign along the spanwise direction, which is consistent with previous reports (*e.g.* Wu *et al.* 1996), and are apparently the manifestation, in the (*x*, *z*)-plane, of the longitudinal vortices. Note that the value of $\omega_{y,\max}^*$ is quite comparable with that of $\omega_{z,\max}^*$. For $x^* > 4$, the transverse vorticity concentrations appear irregular for all examined *Re*. However, the spanwise-averaged vorticity (Figure 3.8d ~ f), *i.e.* $\hat{\omega}_y^* = \frac{1}{N}\sum_{j=1}^{N}\left|\omega_{y,j}^*\right|$, where $N = 63$ is the total number of ω_y^* data at a given x^* along the span, displays a periodic variation along the *x* direction. To better understand this variation, the streamwise velocity *U* is also spanwise averaged, *i.e.*, $\hat{U}^* = \frac{1}{N}\sum_{j=1}^{N}U_j^*$. The longitudinal distance between two adjacent $\hat{U}^*$ peaks is around 4*d*, about the same as the wavelength of the spanwise vortices. This coincidence is reasonable because the peak and the valley of $\hat{U}^*$ should correspond longitudinally the centers of negative and positive spanwise vortices, respectively (see Fig. 9a in Zhou *et al*. 2002). The peaks of $\hat{\omega}_y^*$ tend to correspond to either the peak or the valley of $\hat{U}^*$. While the peak of $\hat{U}^*$ may arise from the three dimensionality of the spanwise vortices, the valley may be due to the occurrence of the longitudinal vortices. A conceptual sketch between the two types of vortices is given in Figure 3.9a.

The spatial relationship between spanwise and longitudinal vortices in the measured plane may be examined by plotting the longitudinal location ($x_{\omega y}^*$) of the $\hat{\omega}_y^*$ peaks, arising from the longitudinal vortices (excluding those due to the three dimensionality of the spanwise vortices), and that ($x_{\omega z}^*$) of the $\hat{U}^*$ peaks. Figure 3.9b indicates that $x_{\omega y}^*$ and $x_{\omega z}^*$, averaged from 200 PIV images measured at $y^* = 0.5$, are linearly correlated, viz.

$$x^*_{\omega y} = x^*_{\omega z} - C\,, \tag{3-4}$$

where C is 0.52, 0.22 and 0.15 for Re = 2000, 5000 and 10000, respectively. The variation in C, as Figure 3.9b indicates, may imply a change in the relative position between the spanwise and longitudinal vortices and hence in the orientation of the longitudinal vortices.

Figures 3.8a ~ c further suggest that the row of the ω^*_y concentrations, which is nearest to the cylinder, occurs closer to cylinder at higher Re. Given the longitudinal structures wrap around the spanwise vortices (*e.g.* Bernal & Roshko 1986 and Zhang *et al.* 2000), the observation is consistent with the fact that vortex formation length reduce with Re. Define the streamwise centroid of transverse structures in the (x, z)-plane similarly to that, Eq. (3-1), of spanwise structures, viz.

$$x_c = \frac{1}{\Gamma_y}\int_A x\omega_y dA\,. \tag{3-5}$$

Figure 3.10 shows the histograms of the centroid position of detected transverse structures in the (x, z)-planes at y^* = 0 and 0.5. The peak indicates the most likely occurrence position of the transverse structures, and reconfirms that the vortex formation length reduces for a higher Re. Apparently, the peak at y^* = 0.5 occurs further downstream, compared with that at y^* = 0, which is consistent with the orientation of the longitudinal structures (Figure 3.9a). Based on this difference, the most likely orientation of the longitudinal structures can be estimated, viz.

$$\theta = \tan^{-1}\frac{\Delta y}{\Delta x} = \tan^{-1}\frac{0.5d}{x_c(0.5) - x_c(0)}\,. \tag{3-6}$$

Thus determined θ is 48° at *Re* = 2,000, 46° at *Re* = 5,000 and 43° at *Re* = 10,000, which are quite close to Wu *et al.*'s (1996) estimate of 47° at *Re* = 544 in the near wake ($x^* < 4$). Further downstream this inclination angle seems increasing. For example, Hayakawa & Hussain (1989) reported 60° at $x^* = 10$ for *Re* =130000, and Zhou & Antonia (1994a) measured 55° at $x^* = 20$ for at *Re* = 5600.

By the definition of the effective area of a vortical structure in Section 3.3, cut-off at 10% of peak vorticity, the averaged extent of transverse structures is estimated to be $\overline{d}_x^* \approx 0.62$ in the *x*-direction and $\overline{d}_z^* \approx 0.47$ in the *z*-direction, irrespective of the *Re* or y^* values. An appreciably larger d_x^* than d_z^* is because of the inclination of the transverse structures, e.g. 43° at *Re* = 10,000, with respect to the *x*-axis. The product of $d_x^* \cdot \cos(43°)$ yields 0.45, that is, the cross-section of longitudinal vortices may be considered as approximately round-shaped. The averaged wavelength $\overline{\lambda}_z^*$ between the centroids of the adjacent same-sign transverse structures is about 1.1 along the spanwise direction, which is consistent with Williamson's (1995) and Wu *et al.*'s (1994a) suggestion that λ_z^* for mode B was of the order of 1.

The averaged maximum vorticity, $\overline{\omega}_{y,\max}^*$, associated with the transverse structures, increases with *Re* and is irrespective of (*x*, *z*)-planes, as listed in Table 1. So does the averaged circulation, $\overline{\Gamma}_y^*$, for the transverse structure. The observation is consistent with previous reports (Norberg 1998; Prasad & Williamson 1997;

Zhou *et al.*2003) that the activities of small-scale structures increase with *Re*, in particular, when *Re* exceeds 5000.

Table 3.1 Averaged maximum vorticity and circulation of transverse structures

Re	y^*	2000	5000	10000
$\overline{\omega}^*_{y,\max}$	0	1.33	1.38	1.43
	0.5	1.70	1.89	2.03
$\overline{\Gamma^*_y}$	0	0.3	0.34	0.37
	0.5	0.36	0.40	0.45

3.5 Streamwise Structures

The typical iso-contours of streamwise vorticity, ω_x^*, measured in the (*y*, *z*)-plane at x^* = 5 for *Re* = 2000, 5000 and 10000, are presented in Figures 3.11 (a), (b) and (c), respectively. The cut-off level, $|\omega_x^*|$ = 0.30, of the ω_x^* contours is still 10% of the maximum streamwise vorticity ($\omega^*_{x,\max}$). This level and the contour increment are same for the three examined Reynolds numbers. The two horizontal parallel solid lines at the center of each figure indicate the cylinder position. The concentrations of ω_x^* with alternatively arranged signs occur in one row. This vortical pattern is similar to that observed, in the close proximity to the cylinder, in the (*x*, *z*)-plane. Apparently, the concentrations are the signature of the longitudinal structures in the (*y*, *z*)-plane. Figures 3.11d ~ f present the lateral distribution of the spanwise-averaged $\hat{\omega}_x^*$, *i.e.* $\hat{\omega}_x^* = \frac{1}{N}\sum_{i=1}^{N}\left|\omega^*_{x,i}\right|$, and spanwise-averaged $\hat{V}^*$, *i.e.*

$\hat{V}^* = \frac{1}{N}\sum_{i=1}^{N} V_i^*$, where N = 79 is the total number of ω_x^* data along the span. The peak of $\hat{\omega}_x^*$ indicates approximately the most probable position of the ω_x^* concentrations for the instant captured by PIV, whereas the $\hat{V}^*$ peak corresponds to the spanwise vortex centre. The positive or negative $\hat{V}^*$ corresponds to an upward or downward lateral velocity component. In general, given the $\hat{\omega}_x^*$ peak occurs above the centerline, a positive $\hat{V}^*$ peak can occur either above the centerline (*e.g.* Figure 3.11d ~ f) or below the centerline (associated with a spanwise vortex below the centerline, not shown). On the other hand, the $\hat{\omega}_x^*$ peak that occurs below the centerline is associated with a negative $\hat{V}^*$ peak above or below the centerline (not shown). The observations are internally consistent with the relative position between $x_{\omega_z}^*$ and $x_{\omega_y}^*$ (Figure 3.9b) as well as the way the streamwise vortices wrap around the spanwise vortices (Figure 3.9a). The observations further suggest that the streamwise vortices tend to occur longitudinally near the upstream spanwise vortex on the other side of the wake.

In the (*x*, *z*)-plane for $x^* > 4$, it is difficult to recognize the alternate pattern of oppositely signed transverse structures, for example Figure 3.8a ~ c. The alternate nature of oppositely signed streamwise structures in the (*y*, *z*)-plane is however more persistent and identifiable even at x^* = 10 (Figure 3.12a) and 15 (Figure 3.12b), though its regularity is increasingly weakened with x^*. At x^* = 20, this alternate nature is difficult to recognize, as shown in the iso-contours of ω_x^* in

Figure 3.12c, which is typical among the 200 images examined. The observation suggests the breakup of longitudinal structures by $x^* = 20$. Note that the same cutoff level of the ω_x^* contours and increment have been used for $x^* = 10$, 15 and 20 in Figure 3.12. It appears that, while the maximum streamwise vorticity decreases with x^*, the streamwise structures grow laterally up to $x^* = 15$, probably under the effect of turbulent diffusion. These elongated structures tend to be 'multipolar', which is not so visible in Figure 3.12c, probably due to vortex breakup.

By the earlier definition of the extent of a vortical structure, the averaged extent of the streamwise structure in the *(y, z)*-plane is given in Figure 3.13 in terms of $\bar{d}_y^*$ in the y-direction and $\bar{d}_z^*$ in the *z*-direction. As x^* increases, both $\bar{d}_y^*$ and $\bar{d}_z^*$ grow slowly and almost linearly. However, the probability density functions, p.d.f. (d_y^*) and p.d.f. (d_z^*) at $Re = 2000$ (Figure 3.14), of d_y^* and d_z^*, show the peak at $d_{y,peak}^* = 0.63$ and $d_{z,peak}^* = 0.47$, respectively, for all x^* positions, that is, the most likely size of the streamwise vortex does not vary with x^*. The gradual rise in $\bar{d}_y^*$ and $\bar{d}_z^*$ (Figure 3.13) is ascribed to a reduction in the number of smaller-size streamwise structures, as evident in Figure 3.14. For all examined *Re*, $\bar{d}_y^*$ is always larger than $\bar{d}_z^*$, though the ratio, $\bar{d}_y^* / \bar{d}_z^*$, remains almost unchanged for all x^*. The difference between $\bar{d}_y^*$ and $\bar{d}_z^*$ is apparently because the streamwise vortices are inclined to *x*-axis. As a matter of fact, the most likely d_z^* is the same as that (0.47) estimated in the (*x*, *z*)-plane.

The spanwise wavelength λ_z^* may be estimated based on the distance between the centroids of the adjacent streamwise structures of the same sign. The averaged wavelength $\overline{\lambda}_z^*$ at $x^* = 5$ is about 1.14 for all three *Re* (Figure 3.15). This estimation agrees with the values reported in the literature. Mansy *et al*. found $\overline{\lambda}_z^*$ to be proportional to $\mathrm{Re}^{-0.5}$ for $Re = 300 \sim 2200$. Wu *et al.*'s (1994a) data also showed that $\overline{\lambda}_z^*$ is *Re* dependent. However, Williamson *et al*. (1988) suggested that $\overline{\lambda}_z^*$ was independent of *Re* within range $Re = 5000 \sim 10000$. Present data suggest a conclusion same to Williamson's. An appreciably higher *Re* range could be responsible for the difference in terms of the *Re* dependence between the present measurement and Mansy *et al.*'s and Wu *et al.*'s data.

In Figure 3.16a, it can be observed that the maximum vorticity $\overline{\omega}_{x,\max}^*$ of streamwise structures decays rapidly and almost linearly from $x^* = 5$ to 10 and less so, albeit linearly, for $x^* > 10$. The circulation $\overline{\Gamma_x^*}$ (Figure 3.16b) associated with streamwise structures decays in a similar trend. It seems plausible that the adjacent opposite-signed streamwise structures are close to each other at $x^* = 5 \sim 10$, which is corroborated by the ω_x^* contours in Figures 3.11a ~ c and 12a, and thus interact vigorously, resulting in the cancellation of opposite-signed vorticity and a rapid decay in streamwise vorticity. At $x^* > 10$, such an interaction impairs due to the breakup of streamwise structures. The decay in $\overline{\omega}_{x,\max}^*$ therefore is less rapid. If extrapolated, $\overline{\Gamma_x^*}$ is compared favourably with Lin *et al.*'s (1995a) and Chyu *et* *al.*'s (1996) data. Brede *et al.*'s data is slightly smaller than the present estimate at *Re* = 2000. Considering the *Re* effect, agreement is also quite good.

3.6 Conclusions

The spanwise and longitudinal structures in the near wake of a circular cylinder have been investigated by PIV technique. The investigation leads to the following conclusions.

1. The modified PIV, with one of the two light sheets pre-displaced, proves to be reliable for the measurement of longitudinal structures in the near wake, at least from $x^* = 5$ up to $x^* = 20$, within a *Re* range of 2000 to 10000.
2. The longitudinal structures are distinct in size, strength and downstream evolution from the spanwise vortices. Given a cut-off level of 10% of the maximum vorticity, the former has a dimension of about 0.5*d*, one fifth that of the latter. Its circulation is about one sixth that of the latter. Whilst the latter breaks up at $x^* \approx 40$ (*e.g.* Zhou & Antonia 1993), it is difficult to detect the alternate arrangement of the positive and negative streamwise structures in the (y, z)-plane at $x^* > 15$.
3. An alternative definition for the vortex formation length is proposed based on the spanwise vortex growth in size. Under this definition, the vortex formation length shrinks with increasing *Re* for the *Re* range investigated, as well documented in the literature. Thus determined

length is however larger than that based on the maximum streamwise fluctuating velocity (Bloor 1964).

4 The present measurement agrees with and complement with the data available in the literature in terms of the convection velocities, trajectory and strength of spanwise vortices in the near wake of a circular cylinder. Within the vortex formation length, the streamwise convection velocity of spanwise vortices increases from about 0.6 at x^* = 3 to 0.7 at x^* = 5 and, meanwhile, the lateral convection velocity drops approximately linear from 0.14 to near zero. Furthermore, the maximum spanwise vorticity follows a linear decay within the vortex formation region. This decay is appreciably slower beyond this region.

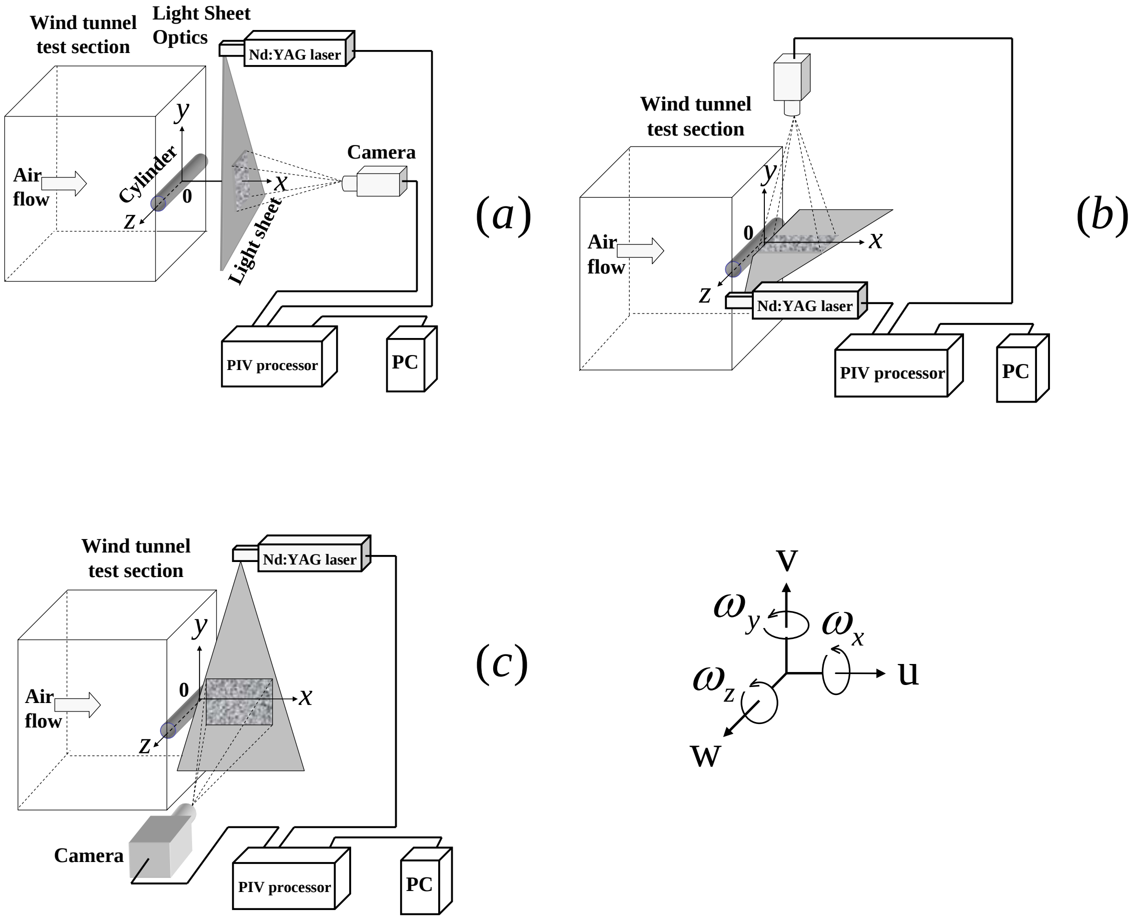

Figure 3.1 Experimental arrangement for the measurement of (a) streamwise vorticity ω_x , (b) transverse vorticity ω_y , (c) spanwise vorticity ω_z .

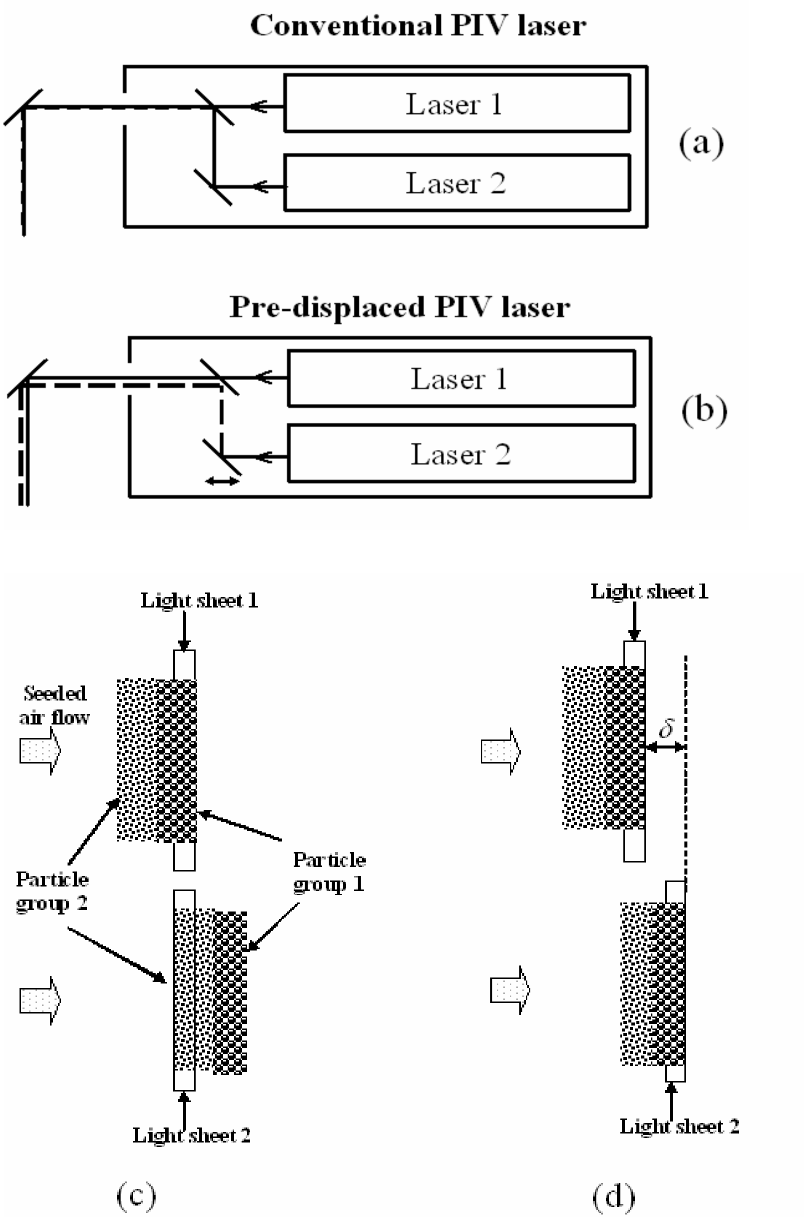

Figure 3.2 Special light sheet arrangement for the PIV measurement of ω_x: (a) conventional PIV laser; (b) pre-displaced PIV laser with shifted mirror; (c) conventional light sheet arrangement; (d) pre-displaced light sheet arrangement.

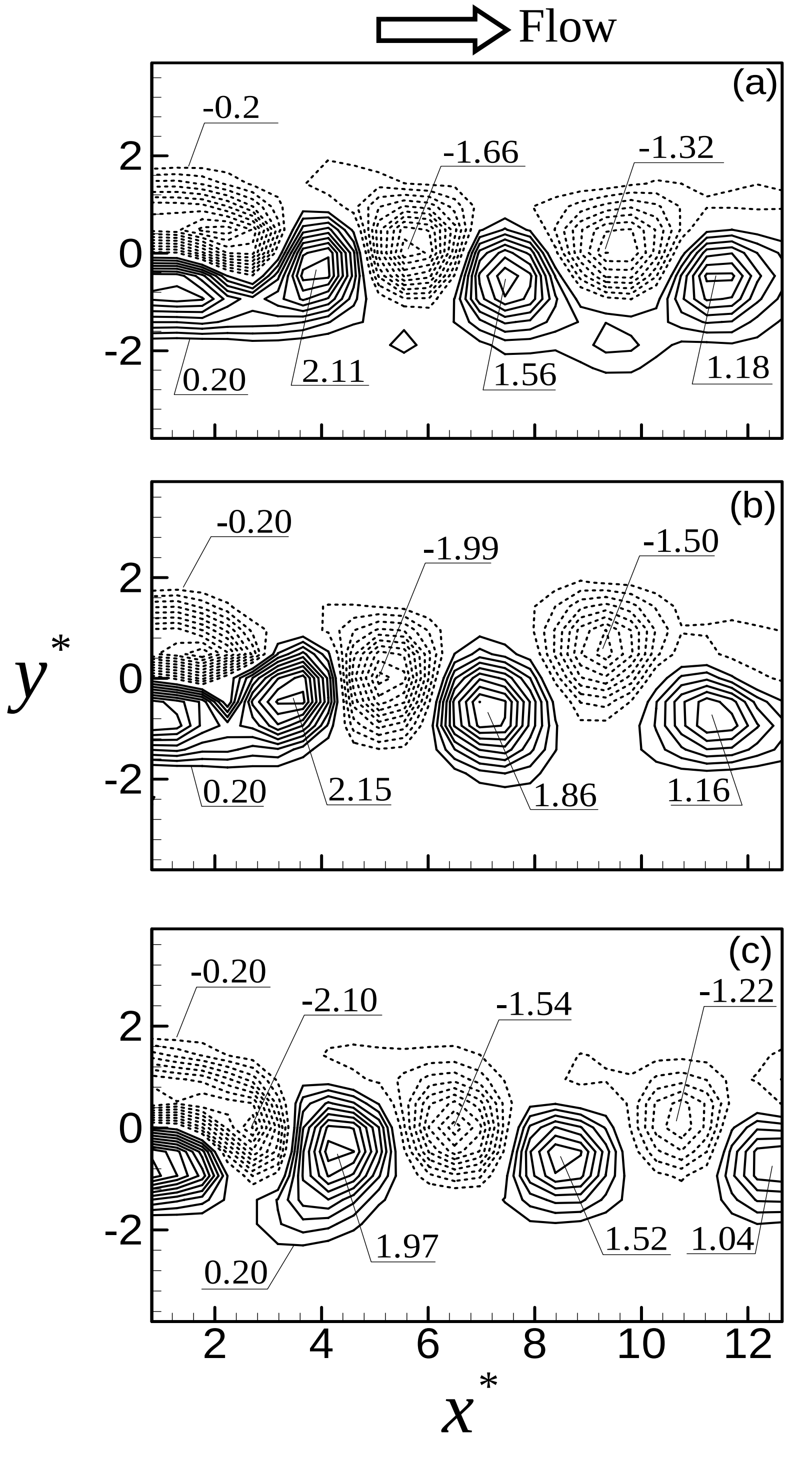

Figure 3.3 The iso-contours of ω_z^*. (a) Re = 2000, (b) 5000, (c) 10000. The cut-off level $|\omega_z^*|$ = 0.20, the increment $\Delta\omega_z^*$ = 0.20.

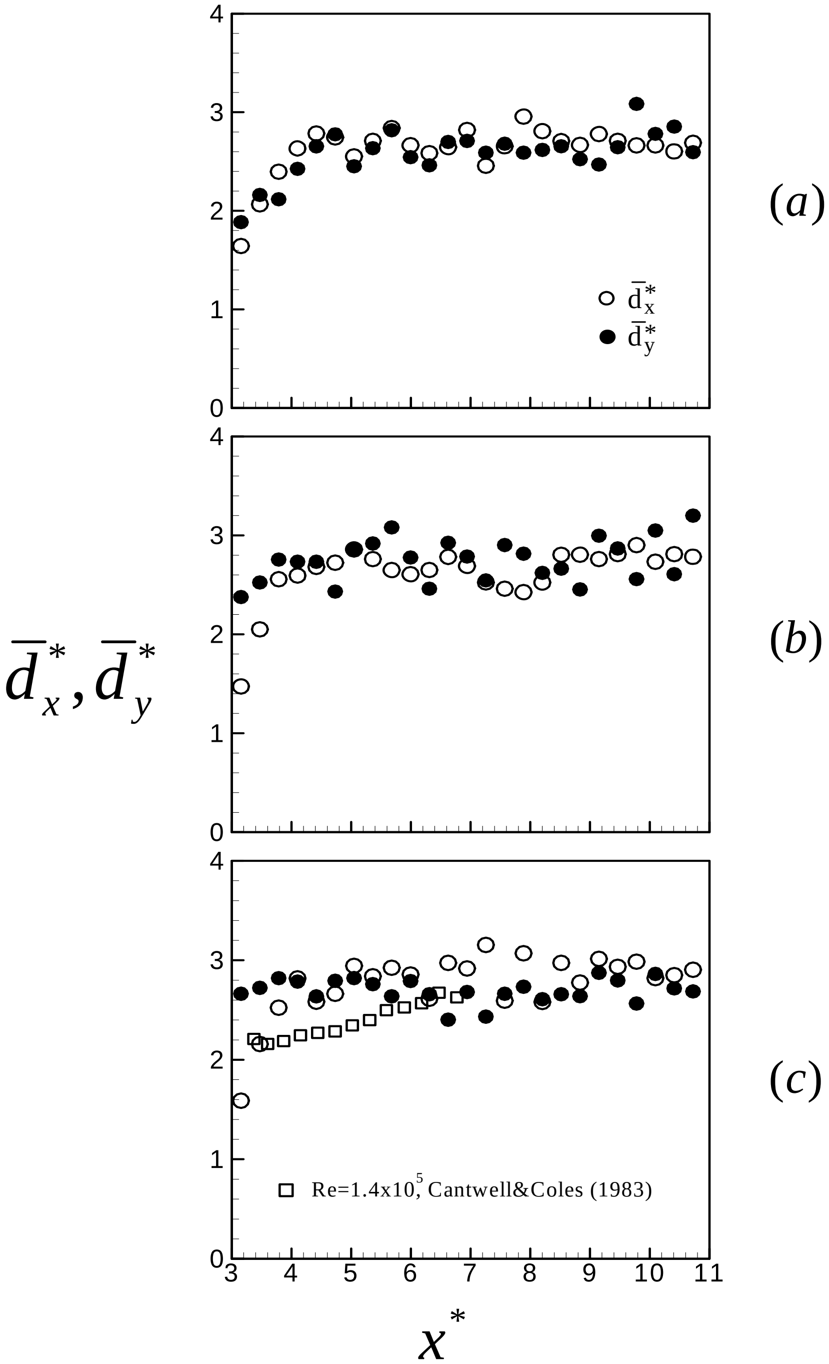

Figure 3.4 Variation of the spanwise vortex size, $\overline{d}_x^*$ and $\overline{d}_y^*$, with x^*:

(a) *Re* = 2000, (b) 5000, (c) 10000.

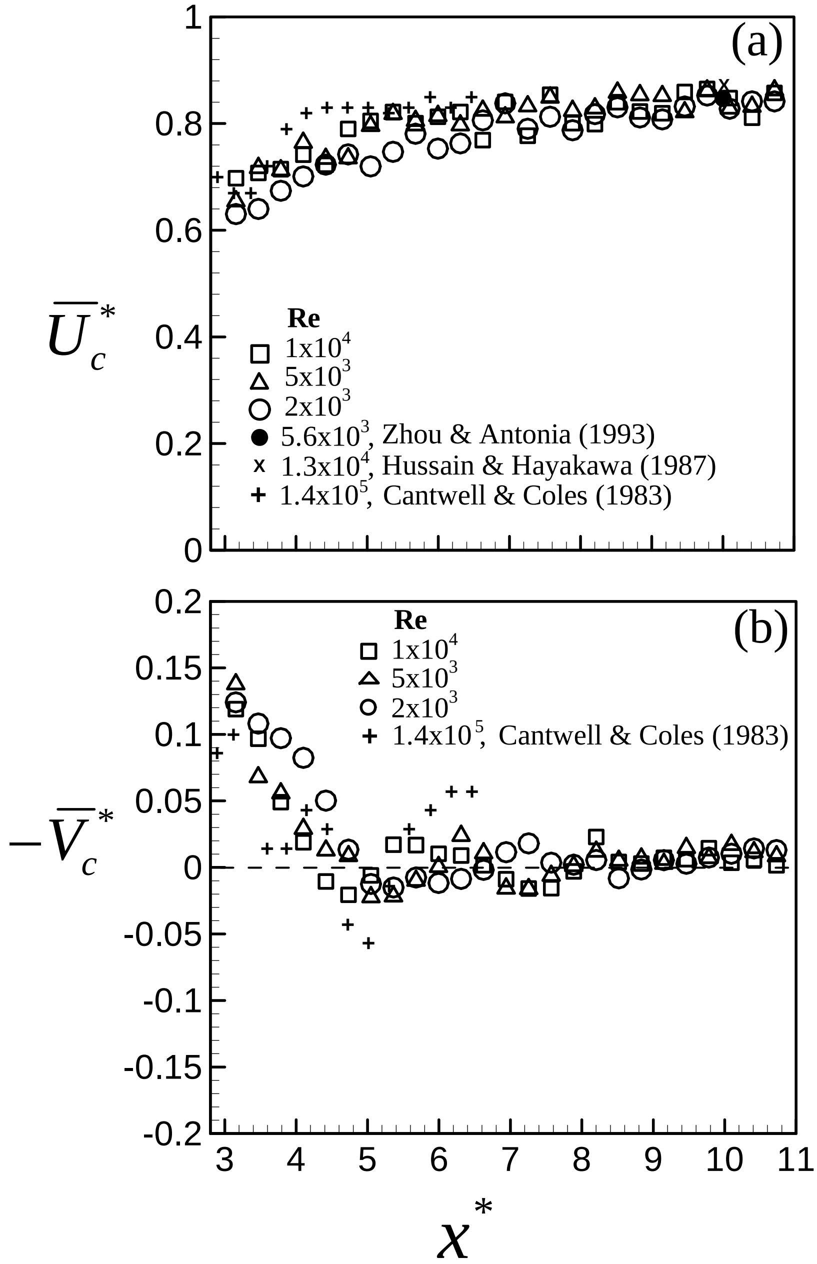

Figure 3.5 Averaged convection velocity of negative spanwise vortices above the centerline: (a) $\overline{U}_c^*$, (b) $\overline{V}_c^*$.

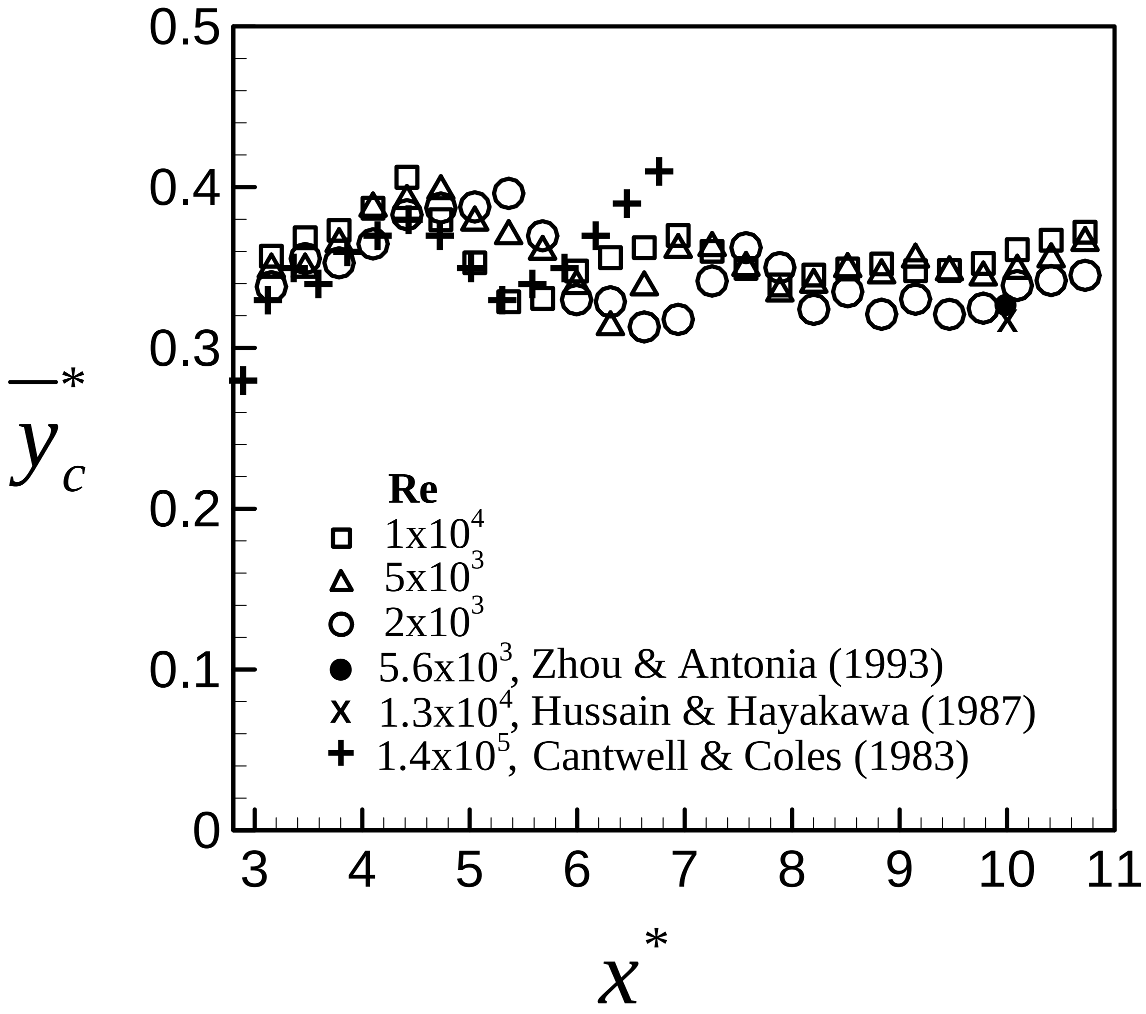

Figure 3.6 Trajectory of spanwise vortices.

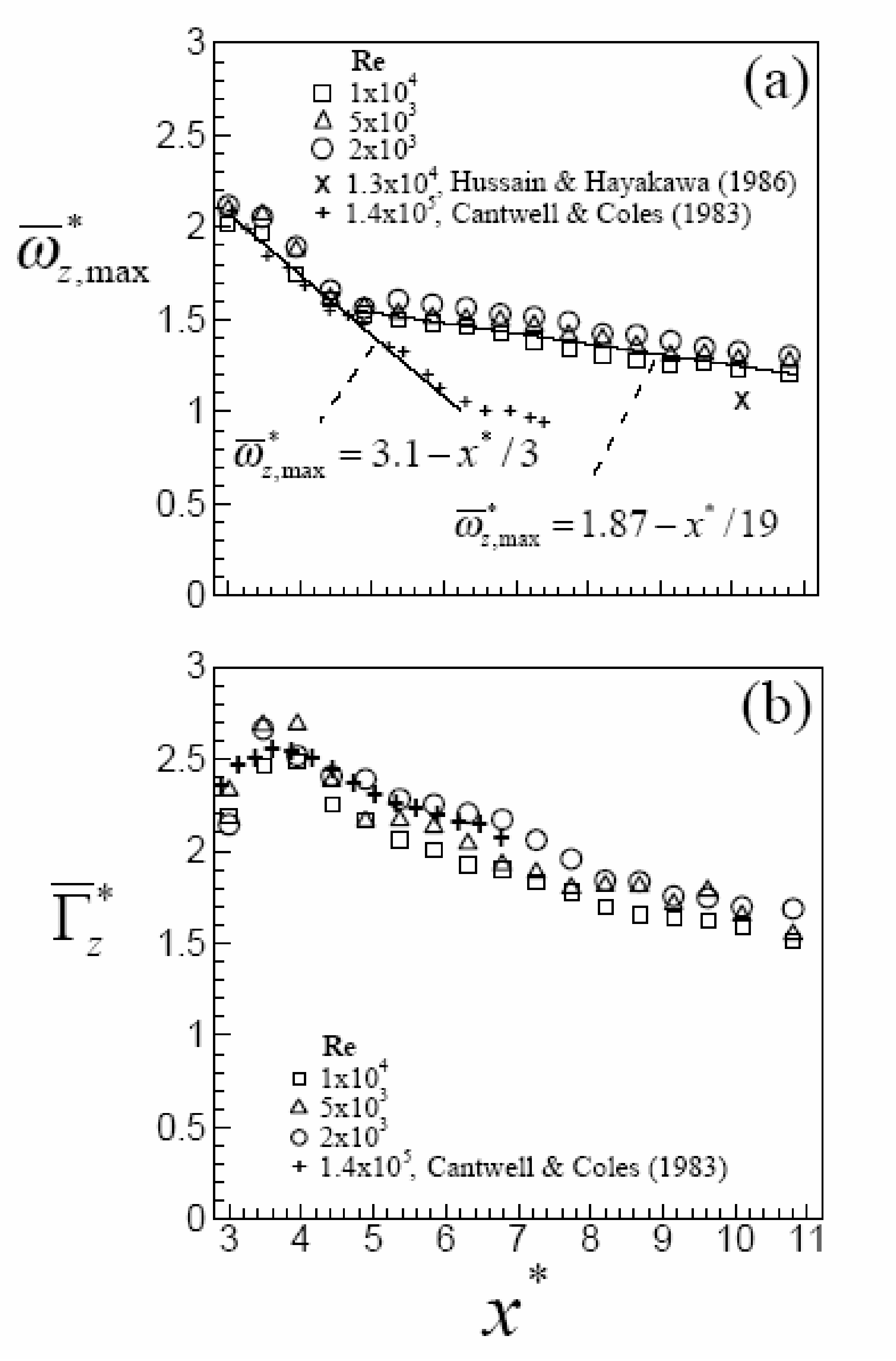

Figure 3.7 Dependence on x^* of (a) the maximum vorticity $\omega^*_{z,\max}$ and (b) circulation Γ^*_z associated with the spanwise vortex.

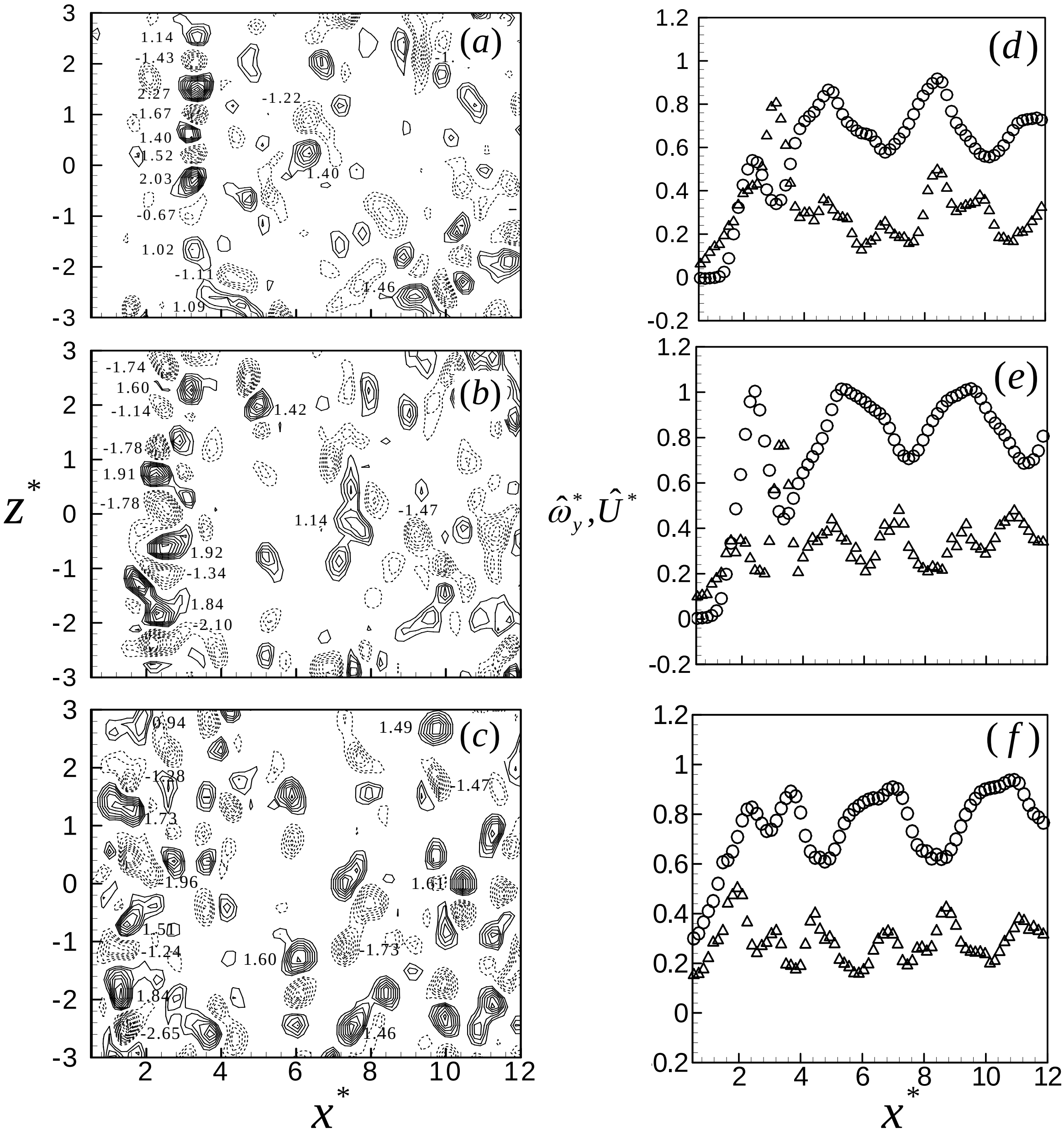

Figure 3.8 The ω_y^*-contours at y^* = 0.5 and the corresponding spanwise-averaged vorticity $\hat{\omega}_y^*$ (Δ) and streamwise velocity $\hat{U}^*$ (O). The cut-off level $|\omega_y^*|$ = 0.20 and the contour increment $\Delta\omega_x^*$ = 0.20. (a) and (d) *Re* = 2000; (b) and (e) 5000; (c) and (f) 10000.

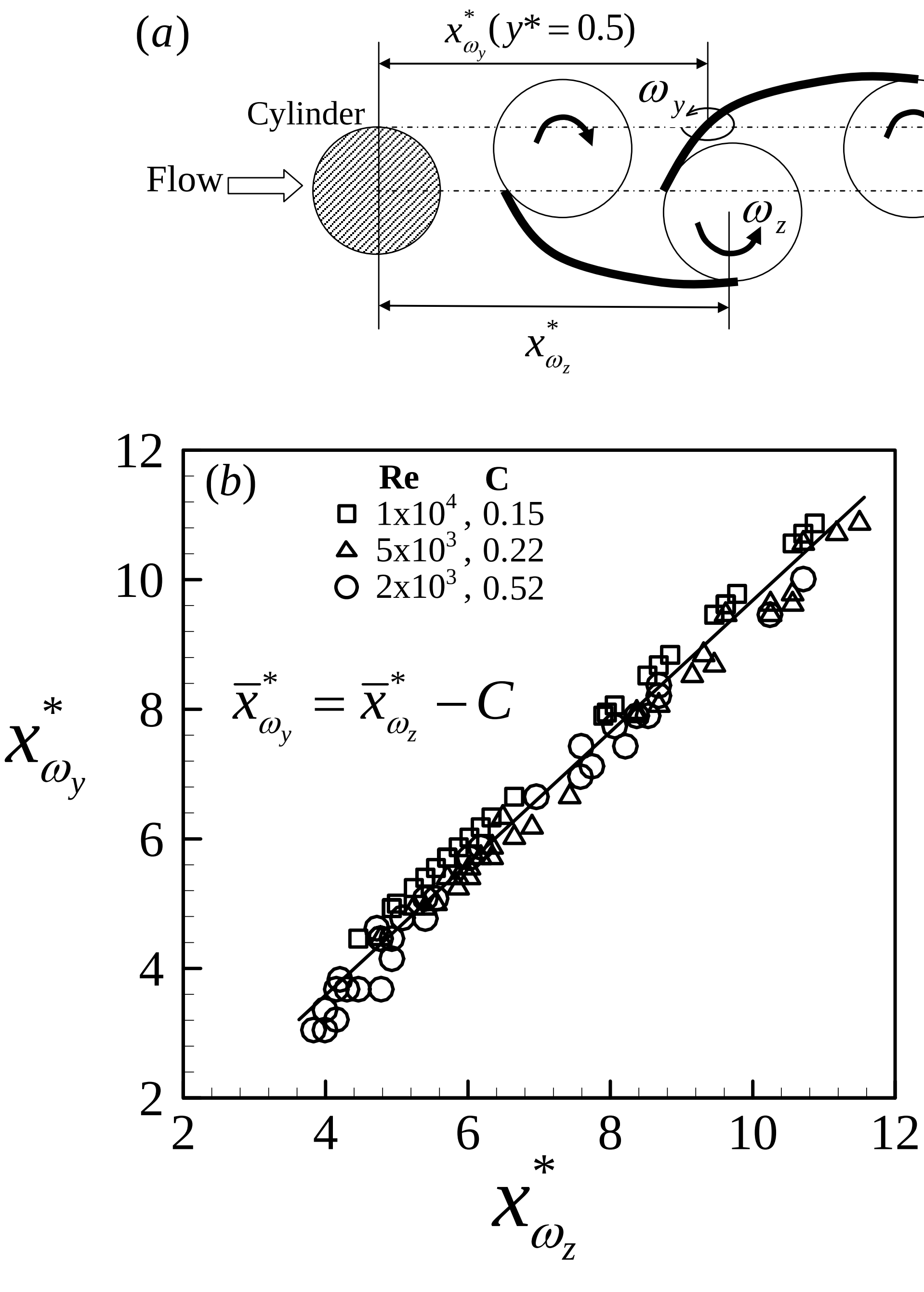

Figure 3.9 (a) Conceptual sketch of spanwise and longitudinal vortices, (b) correlation between the centroids positions of spanwise and longitudinal vortices in the (x, z)-plane at $y^* = 0.5$.

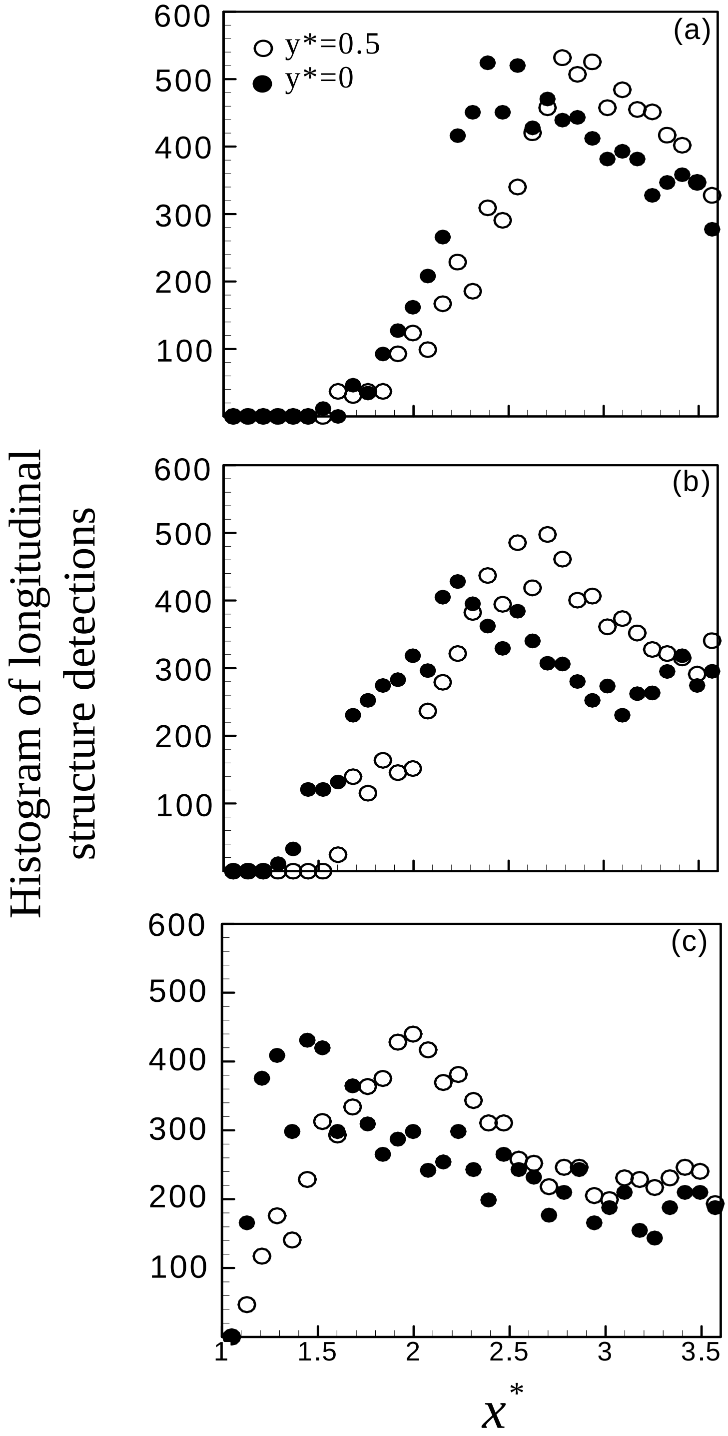

Figure 3.10 Histogram of longitudinal structure detections in the (x, z)-plane at y^* = 0 and 0.5: (a) Re = 2000; (b) 5000; (c) 10000.

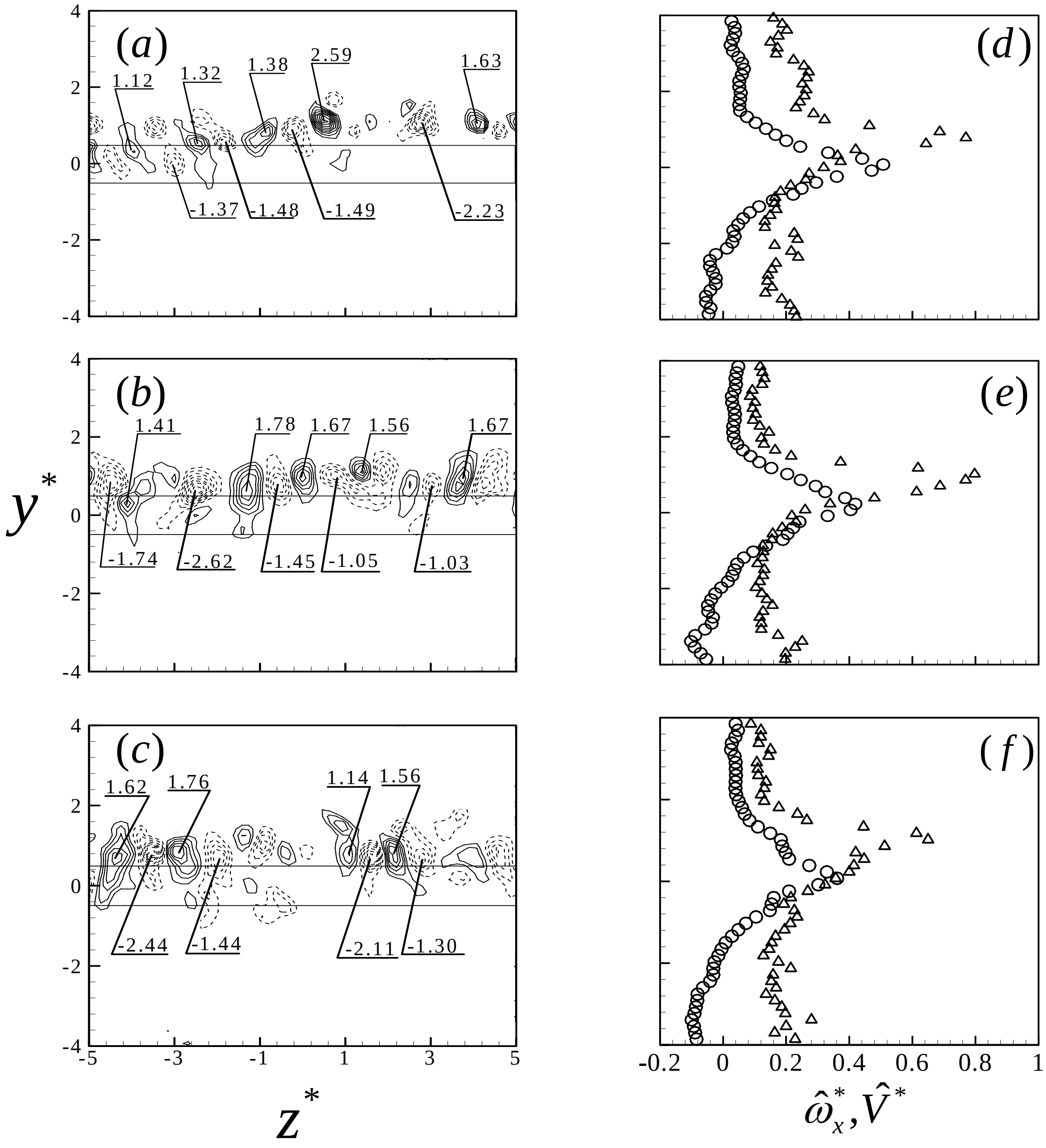

Figure 3.11 The ω_x^*-contours at x^* = 5 and the corresponding spanwise-averaged vorticity $\hat{\omega}_x^*$ (Δ) and lateral velocity $\hat{V}^*$ (O). The cut-off level $|\omega_x^*|$ = 0.30 and the contour increment $\Delta\omega_x^*$ = 0.30. The horizontal parallel solid lines indicate the cylinder position. (a) and (d) *Re* = 2000; (b) and (e) 5000; (c) and (f) 10000.

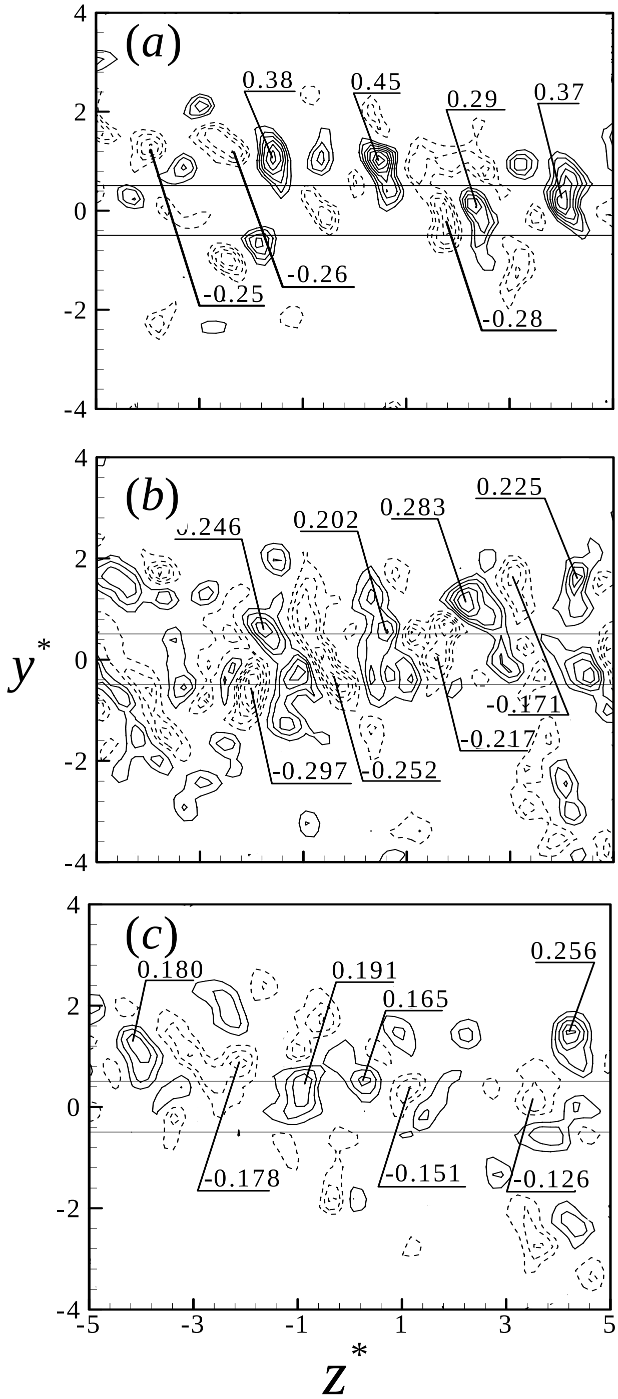

Figure 3.12 The ω_x^*-contours at *Re* = 5000, the cut-off level $|\omega_x^*|$ = 0.05, the contour increment $\Delta\omega_x^*$ = 0.05: (a) x^* = 10, (b) 15, (c) 20.

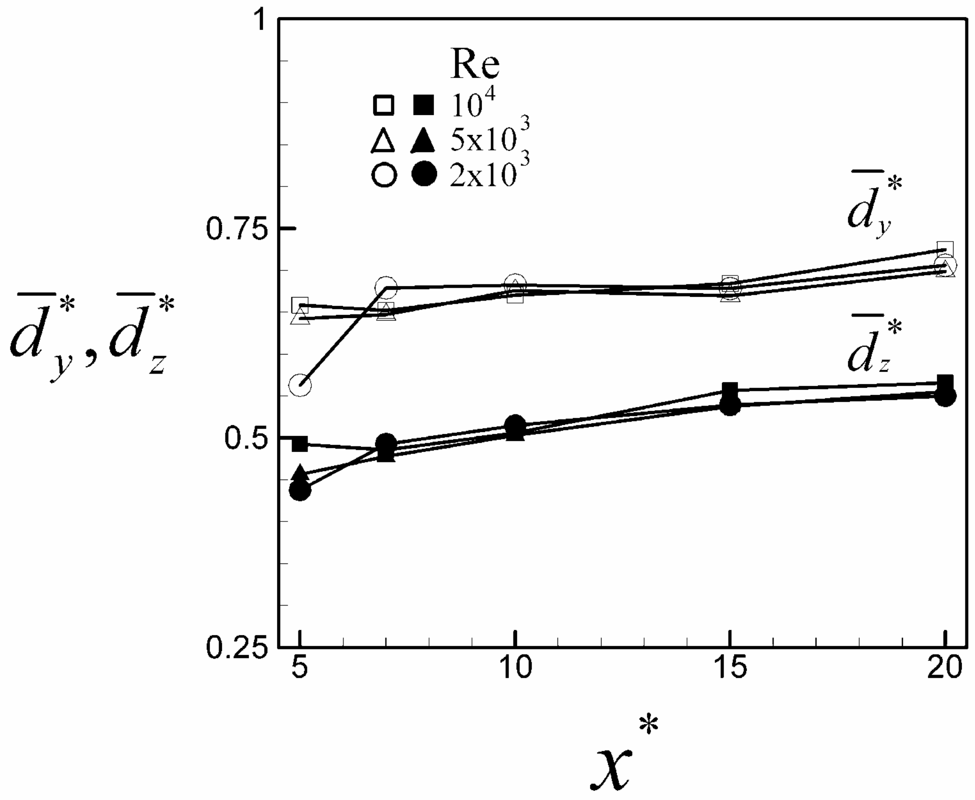

Figure 3.13 Spanwise and lateral sizes of streamwise structures in the (y, z)-plane.

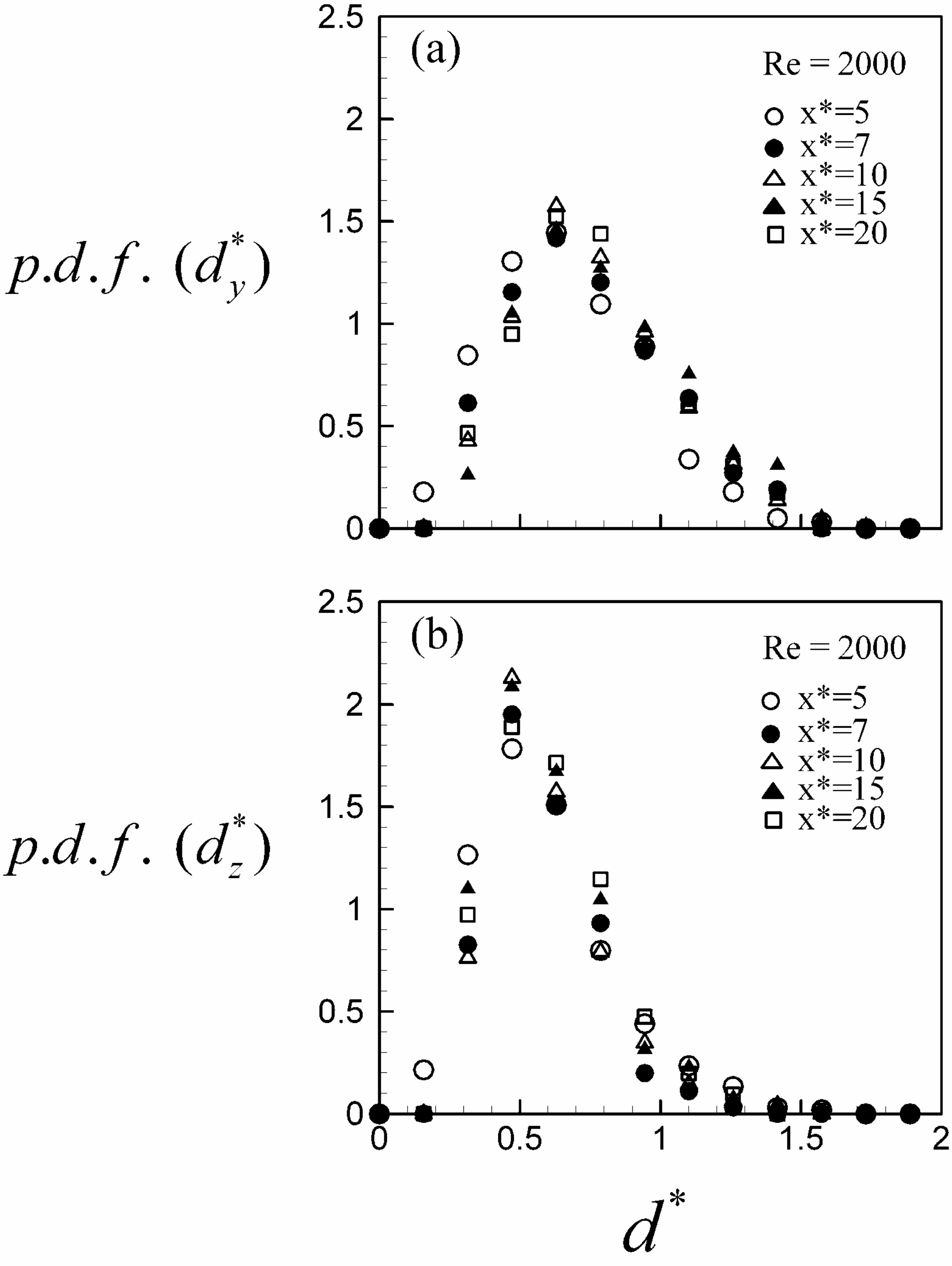

Figure 3.14 Probability density function of (a) d_y^* and (b) d_z^*.

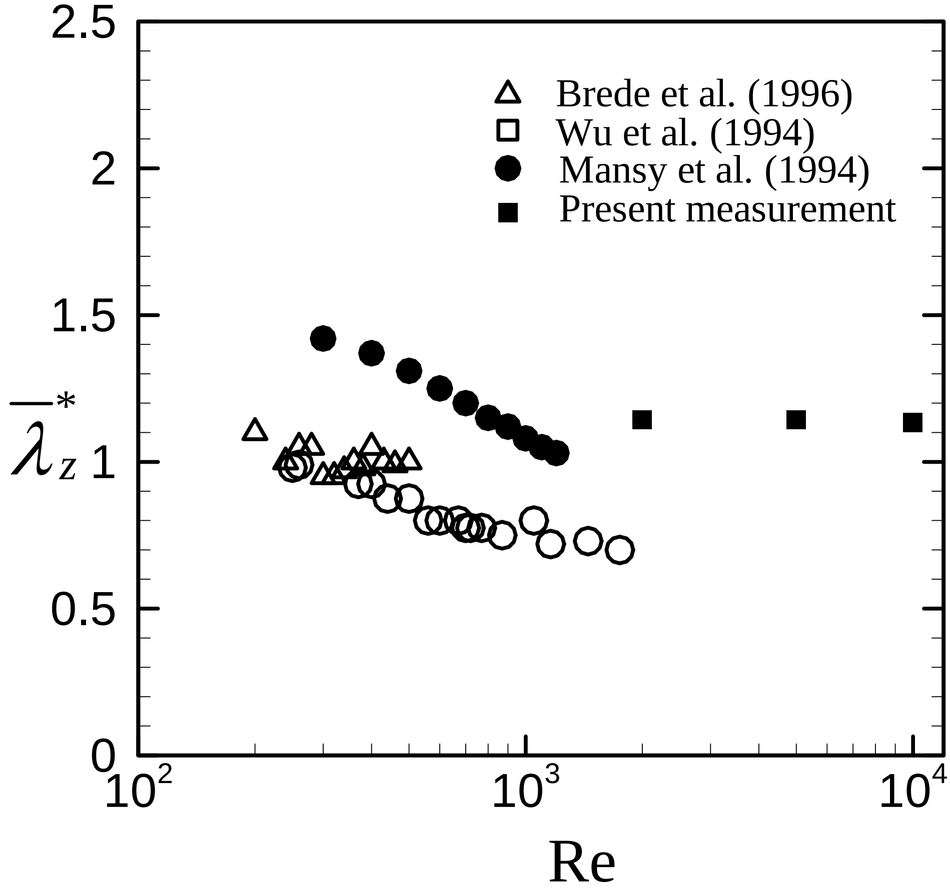

Figure 3.15 Spanwise wavelength of streamwise vortices estimated at $x^* = 5$.

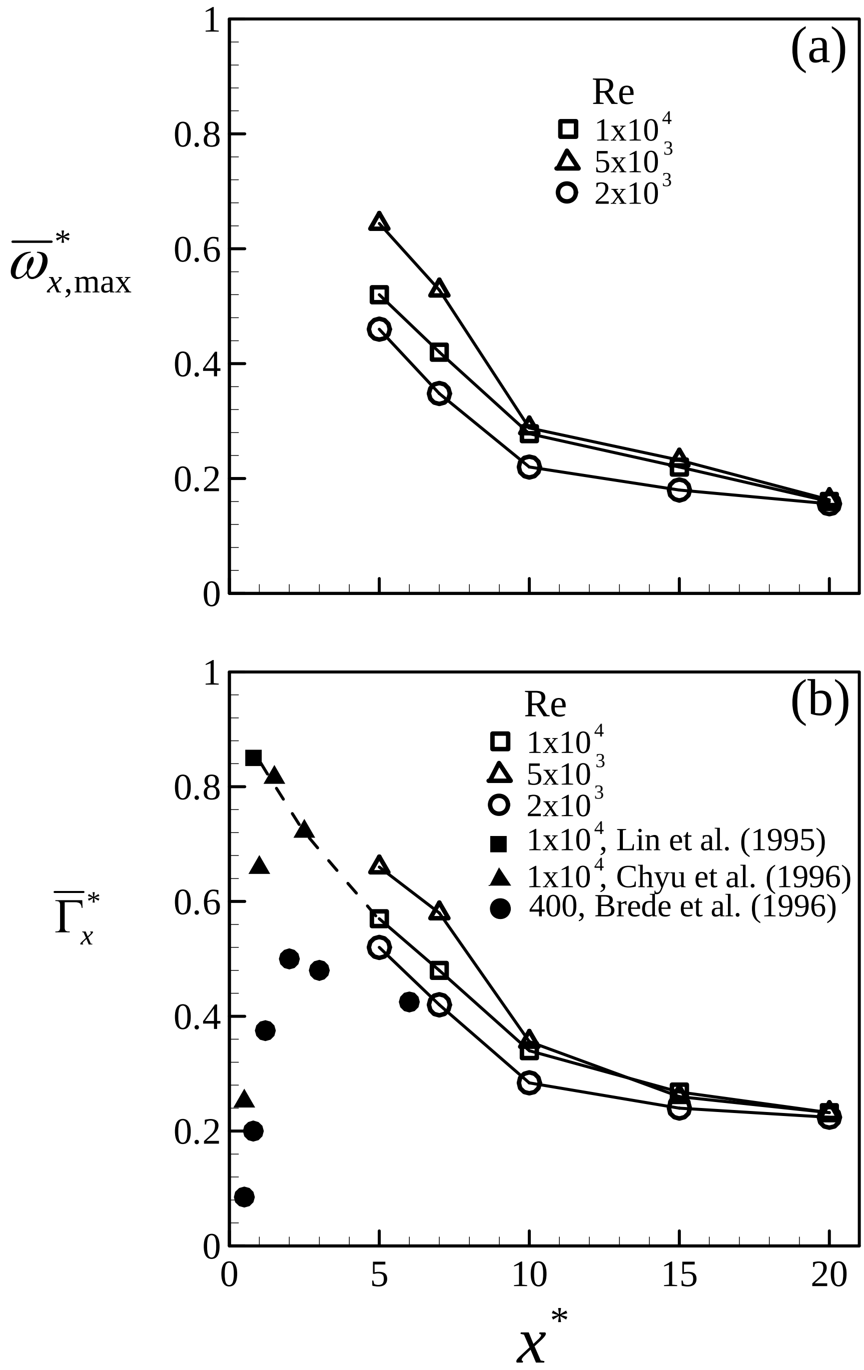

Figure 3.16 Streamwise evolution of (a) the maximum streamwise vorticity $\overline{\omega}^*_{x,\max}$ and (b) circulation $\overline{\Gamma}^*_x$.

Chapter 4: Fluid dynamics around an inclined cylinder with running water rivulets

4.1 Introduction

In Chapters 3, the three-dimensional wake structure for a smooth cylinder was presented. This chapter aims to improve our understanding of fluid dynamics associated with an inclined stationary cylinder with running water rivulets, and to develop our understanding of the effects of water rivulets on the near-wake fluid dynamics. Specifically, measure and compare the near-wake of an inclined cylinder, with and without the presence of water rivulets; investigate the three dimensional characteristics of the flow around the cylinder, especially interactions between Karman vortices and longitudinal structures. The non-linear coupling between fluid dynamics and structural dynamics associated with the rain-wind-induced cable vibrations will be investigated in a follow-up work.

4.2 Experimental details

Experiments were carried out in a closed circuit wind tunnel with a working section of $L \times W \times H$ = 2 m × 0.6 m × 0.6 m. Window made of optical glass was applied to maximize the signal-to-noise ratio. The maximum wind speed in the working section was 50 m/s and the longitudinal turbulence intensity was <0.5%. The cable was modeled by a rigid polyethylene-coated acryl glass tube of 0.6 m in length (for such a length, even the real flexible cables would be rather rigid). Its surface condition is similar to that associated with the real cables which are also covered by an out layer of polyethylene. Two 600 mm long cable models, one with an external diameter, *d*, of 45 mm and the other 19 mm, were used in present research. Their aspect ratios are of 13.3 and 31.6, and corresponding blockages were 7.5% and 3.2%, respectively. The model of the larger diameter was applied for its size close to that of actual cables, and for improved accuracy in identifying the rivulet position on the model surface. On the other hand, the model of smaller diameter had negligible blockage and end effects and was used to investigate the detailed flow structures. End plates were used on both models to further minimize the possible end effect. Our findings can still be extended to long flexible cables, because the model represents a typical piece of whole cable body.

The schematic experimental arrangement is presented in Figure 4.1. The cable model of larger diameter was cantilever-supported. The top end of the cylinder was connected to a small turning plate mounted on the ceiling of the working section through a hinge so that the inclination α and yaw angle β of the cylinder can be adjusted to simulate all possible cases of wind attack. The angles of α, β, and θ (the circumferential angle) are defined in Figure 4.2. The *x*-axis is in the same direction as the incoming wind flow, the *y*-axis is perpendicular to the *x*-axis in the horizontal plane and the *z*-axis is normal to both *x* and *y*. The origin of the coordinate system is defined at the center point of the model axis. The angle $\theta = 0°$ is designated as the major axis on the leeward side of the elliptical cross section A-A' in the (*x, y*)-plane. Water from a water tank was released at the upper end of the cylinder at $\theta = 0°$. To maintain a steady flow rate, the water liquid level H_0 in the tank was maintained at same height throughout experiment. Four flow rates were selected to simulate different rainy conditions, that is, Q = 1.4, 3.0, 6.9 and 8.0 liters/hour, respectively. This was achieved by adjusting a regulator valve. Photos of generated leeward and windward rivulets on cylinder surface are presented in Figure 4.3. Because the thin running water rivulets pass through the wind tunnel quickly, for example only 3-4 seconds inside, the natural evaporation of water under any relative humidity of air during this short period can be ignored, compared with the liters of flow rates.

4.2.1 PIV and flow visualization measurements

A Dantec PIV2100 system, already introduced in section 2.2.1, was used to investigate the near wake of the inclined cylinder in both the horizontal (x, y) plane and a vertical plane cutting through the cylinder axis. The cylinder surface and the wall of tunnel working section hit by the laser sheet were black painted to minimize reflection light for good signal-noise ratio. The flow was seeded by smoke, generated from Paraffin oil, of a particle size around 1 μm in diameter. The CCD camera used for the PIV measurements had a field of view as large as 112 mm × 140 mm, *i.e.* x/d = 1 ~ 6.9 and y/d = ± 3.7 (for d = 19 mm). Part of the cylinder included in PIV images had been masked with a built-in masking function of PIV software before velocity maps were calculated from the images. For image processing, 32 × 32 pixel rectangular interrogation areas with 50% overlap were used. The ensuing in-plane velocity vector map consisted of 79 × 63 vectors, and they were further processed to generate vorticity maps of same spatial resolution.

The spatial resolution for vorticity estimate was about 0.14 *d*. The PIV measurements were conducted at U_∞ = 9 m/s and *Q* = 8.0 liters/hour for $\alpha = 45°$, $\beta = 0°$ and 30°. The corresponding Reynolds number *Re* ($\equiv U_\infty d / \nu$, where ν is the kinematic viscosity of air) was 1.14 × 10^4. More than three hundred images were obtained for each β.

In addition to PIV measurements, laser-illuminated flow visualization was also conducted in the wind tunnel using the visualization function of the PIV system in order to obtain the qualitative information on the flow field. The model of larger diameter was used. The camera was operated in the single frame mode with an observation field of 118 mm × 148 mm, corresponding to *x/d* = 1 - 7.2 and *y/d* = ±3.9.

4.2.2 LDA measurements

The wind tunnel and other experimental conditions for LDA measurements were the same as those used for the PIV. In order to acquire the quantitative information of the rivulet effects on the near wake of the cylinder, a two-component LDA (Dantec Model 58N40 LDA with enhanced FVA signal processor) was used to measure velocities at *x/d* = 3 in the mid horizontal plane, *z* = 0, of the working section (Figure 4.1). The LDA has an elliptic measuring volume of 1.18mm minor axis and 2.48mm major axis. The measured mean velocity was estimated to have an error of less than 3% and the corresponding error for the measured root mean square value was less than 10%. The flow marker was the same as used for the PIV measurement. For each sampling point, 250,000 validated data samples were acquired with a data rate of 0.8k Hz ~ 4k Hz. The LDA system comes with the necessary software for data processing and analysis, and the data, besides the mean velocity field, could be processed to yield information on the Reynolds stresses.

4.3 Cross-flow distributions of mean velocities and Reynolds stresses

Figure 4.4 and 4.5 present the LDA-measured cross-flow distributions of mean velocity $\overline{U}^*$, $\overline{V}^*$, Reynolds normal stresses $\overline{u^2}^*$ and $\overline{v^2}^*$, and shear stress $\overline{uv}^*$ measured in the (x, y) plane at $x/d = 3$ for $\beta = 0°$ and 30°, respectively. In this part, an overbar denotes time averaging and an asterisk indicates normalization by U_∞ and/or d. As expected, the distributions at $\beta = 0°$ in Figure 4.4 are reasonably symmetrical or anti-symmetrical about $y/d = 0$ when without water rivulets. With running water rivulets and $\beta \neq 0°$, the $\overline{U}^*$, $\overline{V}^*$ and $\overline{v^2}^*$ distributions are in distinct asymmetrical shapes, apparently due to the effect of the rivulets. The asymmetry is more appreciable at $\beta = 30°$. This distribution is still rational for below two reasons. Firstly, as earlier observed, the two water rivulets are asymmetrically located at $\beta \neq 0°$. Secondly, the elliptical cross section of the cylinder in the (x, y) plane is asymmetrical about the x-axis at $\beta \neq 0°$ (Figure 4.2).

Note that the wake at $\beta = 0°$ displays asymmetry about $y/d = 0$, mainly in the $\overline{V}^*$ distribution, though not substantially (Figure 4.4b). This phenomenon could not be simply ascribed to experimental uncertainties in LDA measurements, which were estimated to be 3% for the mean velocity measurement. In this case, the two rivulets are supposed to be statistically symmetrically formed on the sides of cylinder. However, given asymmetrical vortex shedding, as suggested by $\overline{uv}^*$ (Figure 4.4e), the two rivulets, which oscillates both circumferentially and axially on surface, do not occur symmetrically at any instant since their motions are affected by the flow separation from the cable. Furthermore, the water released at the top end of the cylinder developed into two rivulets with different mass flow rates. As a consequence of force balance, the positions of the two water rivulets will deviate from the symmetry about *y/d* = 0. The two reasons may explain the observed the asymmetrical distribution in $\overline{V}^*$ (Figure 4.4b).

At $\beta = 0°$, the distributions of $\overline{U}^*$, $\overline{V}^*$, $\overline{u^2}^*$, $\overline{v^2}^*$ and $\overline{uv}^*$ with running water rivulets show appreciable deviation from those without rivulets (Figure 4.4). The $\overline{u^2}^*$ (Figure 4.4c) displays a twin peak distribution in both cases, but the two peaks are more pronounced and farther separated with the presence of water rivulets. This phenomenon suggests that the two water rivulets at cylinder sides result in larger lateral spacing between two rows of oppositely signed vortices than that without the rivulets, which is supported by the PIV data (Figure 4.8). At β = 30° (Figure 4.5), the running water rivulets produces a more significant deviation from that without the rivulets than at $\beta = 0°$, particularly on the cylinder side of *y/d* < 0, where the leeward rivulet occurs. The leeward rivulets apparently induce a significant increase in $\overline{u^2}^*$, $\overline{v^2}^*$ and $\overline{uv}^*$, which is consistent with an increased vortex strength. The observed circumferential oscillation of the leeward rivulet is considerably large, up to $\Delta\theta \approx \pm 15°$ at β = 30°, compared with that of β = 0° while both rivulets remain quite steady with little circumferential oscillation. The results lead to a conclusion that the large circumferential oscillation of the leeward rivulet is mainly responsible for the significant variation in $\overline{U}^*$, $\overline{V}^*$, $\overline{u^2}^*$, $\overline{v^2}^*$ and $\overline{uv}^*$, which conforms to Matsumoto *et al.*'s (2001a) proposition that the leeward water rivulet may dominate the aerodynamic instability. Note that the twin-peak distribution of $\overline{u^2}^*$ (Figure 4.5c) is more evident at β = 30° than at $\beta = 0°$ in the presence of the rivulets.

4.4 Drag of inclined cylinder with running water rivulets

The drag coefficient C_D of a circular cylinder may be estimated by below equation (Antonia and Rajagopalan 1990)

$$C_D = 2\int_{-\infty}^{\infty} \frac{\overline{U}}{U_\infty}\left(\frac{U_\infty - \overline{U}}{U_\infty}\right) d\left(\frac{y}{d}\right) + 2\int_{-\infty}^{\infty} \left(\frac{\overline{v^2} - \overline{u^2}}{U_\infty^2}\right) d\left(\frac{y}{d}\right) \tag{4.1}$$

Based on equation (4.1) and our collected LDA data, estimated C_D was 1.58 and 1.75 at β = 0° and 30°, respectively, with running water rivulets ($\alpha = 45°$), 21% and 34% higher than their counterparts (1.31 at β = 0° and 1.30 at β = 30°) without the water rivulets. This difference between the cases with and without running water rivulets cannot be ascribed to the experimental uncertainty, estimated to be $\pm$4% based on repeated measurements, in determining C_D. The measurement result of increased C_D is consistent with the violent rain-wind-induced cable vibration observed in fields. The enlarged difference at $\beta = 30°$ in C_D between the cases with and without water rivulets further conforms to previous reports that the violent rain-wind-induced cable vibration tends to occur at $\beta = 20°$ - 60° (Yoshimura *et al.* 1988; Flamand 1995).

One remark is due here on the observed drag enhancement in the presence of water rivulets on the inclined cylinder. Bearman and Owen (1998) found that the introduction of wavy separation lines could suppress vortex shedding and hence result in a drag reduction of at least 30%. When projected onto a plane normal to the wind, the present cylinder with water rivulets is also a wavy structure if the rivulets were considered as part of the structure. However, contrary to Bearman and Owen's (1998) wavy structures, this 'wavy' structure does not suppress but enhance the drag. The protuberance induced by rivulets cannot solely account for the presently observed drag increase. Probably the axial and circumferential movement of the water rivulets also contributes to the enhanced drag. This assertion has yet to be verified in future investigations.

4.5 Flow Structures

The flow structures in the (x, y)-plane behind cylinder and a vertical plane cutting through the cylinder axis were investigated by both flow visualization and PIV measurements. In general, the flow in the (x, y)-plane may display an alternate vortex street (Figure 4.6b) or may not (Figure 4.6a), that is, the vortex street occurs intermittently. For instance, about 30% among three hundred flow visualization images examined at $\beta = 0°$ display a vortex street in the absence of water rivulets, but this percentage rises to about 60% in the presence of water rivulets. In the vertical plane cutting through the cylinder axis, the turbulent organized structures are also discernible. For example, at β = 0°, where this plane overlaps with the (x, z)-plane, the flow structure shown in Figure 4.8a is consistent with the quasi-periodical flow separation from the cylinder. Figure 4.8b further shows mushroom-like structures, which are not so evident at β = 30° (not shown) and will be further discussed later along with the vorticity contours.

Figure 4.8 and 4.9 present vorticity contours, $\omega_z^* = \omega_z d / U_\infty$, measured in the ($x$, y)-plane using the PIV technique, when with and without running water rivulets at β = 0° and 30° (α = 45°), respectively. The contours are rather typical for the intermittently observed vortex street. Based on presented PIV data, a number of observations can be made. Firstly, the oppositely signed shear layers may separate symmetrically from the cylinder, as illustrated in Figure 4.8a. The observation is in distinct contrast with alternate vortex shedding from a circular cylinder normal to incident flow. The symmetrical flow separation occurs more frequently in the absence of water rivulets; at β = 30°, this flow structure is recognized in about 25% of images examined without water rivulets but only 15% with the rivulets. The sample size consists of three hundred images for the case with or without rivulets. It is suspected that this difference could have some contributions to the more violent cable vibration in the presence of the water rivulets. Secondly, as β increases from 0° to 30°, there is a remarkable increase in the peak vorticity of vortices with water running rivulets (Figure 4.8b and 4.9b);

the averaged maximum magnitude, statistically calculated from three hundred images, rises by about 50%. Meanwhile, the vortex sizes are rather comparable between the two cases. Therefore it can be inferred that strength of each vortex structure has been significantly increased from β = 0° to 30°. This increase is apparently linked to the increase in C_D from 0° to 30° and probably attributed to an effective cylinder height larger at β = 30° than at β = 0° (refer to Figure 4.2). The result may also provide an explanation for the field observations that the rain-wind-induced vibrations occurs often at a yaw angle of β = 20° - 60° (Yoshimura *et al.* 1988; Flamand 1995). In the absence of water rivulets, however, the averaged maximum vorticity magnitude changes little between the β = 0° and β = 30° cases, for examples the instantaneous vorticity contours in Figure 4.8a and 4.9a. Both are also quite comparable with that with water rivulets at β = 0° (Figure 4.8b). Thirdly, the lateral spacing between oppositely signed vortices enlarges appreciably with running water rivulets present, compared with the case without the rivulets, which is internally consistent with the twin-peak distribution of $\overline{u^2}^*$ (Figures 4.4c and 4.5c). This is probably because the effective cylinder height is increased by the two rivulets at sides.

The three dimensional aspects of flow separation from inclined cylinder may be gained by examining PIV-measured vorticity contours in the vertical plane cutting through the cylinder axis, as shown in Figures. 4.10 and 4.11. This plane overlaps with the (x, z)-plane at β = 0° but not at β = 30°. Note that the abscissa in

Figure 4.11 is denoted by x_β. Use ω_y and ω to represent the measured vorticity in the former and the latter cases, respectively. Interestingly, the ω_y concentrations (Figure 4.10) in the close proximity of the cylinder tend to occur alternately in sign along the axial direction, both with or without the water rivulets, and appear quite similar to the longitudinal vortices observed behind a cylinder normal to the incident flow by current work (Figure 3.8) or by Wu *et al.* (1994). The structures apparently correspond to the mushroom structures seen in Figure 4.7a, or more evident in Figure 4.10 the vorticity contours. Summarized from three hundred photos, the mushroom structure is a dominant feature in wake for inclined cylinder as well. The alternately signed structures seem to be best captured in the (x, z)-plane; they are less evident at β = 30° (Figure 4.11) since the plane of PIV images are not parallel to the (x, z)-plane. Due to the complexities of the present three-dimensional flow, further investigations are needed to clarify the interaction between the longitudinal and Karman vortices.

4.6 Discussions

A scenario of the rain-wind-induced cable vibration may be proposed based on the present data as well as those in the literature. At β = 0°, the vortex street occurs intermittently and the vortex strength is relatively weak, although Verwiebe and Ruscheweyh (1998) did report the rain-wind-induced cable vibration in the case of an almost vertical cable. Thus, it is difficult to induce violent cable vibration when yaw angle β is small. As β increases from 0˚ to 30˚, the strength of vortices rises by up to 60%. In the presence of running water rivulets, shear layer separation from the cylinder tends to be anti-symmetrical and lateral spacing between the oppositely signed vortices enlarges. All these could contribute to an enhanced excitation force on the cylinder, which compromises the significant rise in the mean drag on the cylinder. However, these may not be adequate to account for the violent cable vibration observed in engineering.

Zhang *et al.* (2004) used piezoelectric ceramic actuators to perturb one surface of a square cylinder in a cross flow. The cylinder was spring-supported at both ends. Vortex shedding from the cylinder was in synchronization with the natural frequency of the fluid-structure system. When the surface perturbation, albeit very small in amplitude (only 0.6% of the cylinder height), was made in phase with vortex shedding or the natural frequency of the system through a feedback control system, the vortex strength was doubled and the fluid-structure system damping was significantly reduced. Subsequently the cylinder oscillating amplitude was greatly amplified. The present data reconfirm previous reports that running water rivulets along the cylinder oscillate circumferentially around the flow separation line. Naturally, the rivulets act to perturb or impose a perturbation force on the flow separation. Presumably, their oscillating frequency is the same as the vortex shedding frequency. Given the two frequencies are synchronized with the natural frequency of the fluid-cylinder system (or its harmonics), vortex shedding can be greatly enhanced and the fluid-cylinder system damping will be considerably reduced. As a consequence, the excitation force and hence the cylinder vibrating amplitude may be greatly amplified. Since the present cylinder was very rigid and fix-supported, implying a large damping and negligibly small vibration, the vortex shedding or rivulet oscillation frequency cannot be synchronized with the system natural frequency. Thus, the running water rivulets could only have a very limited effect on the vortex shedding strength.

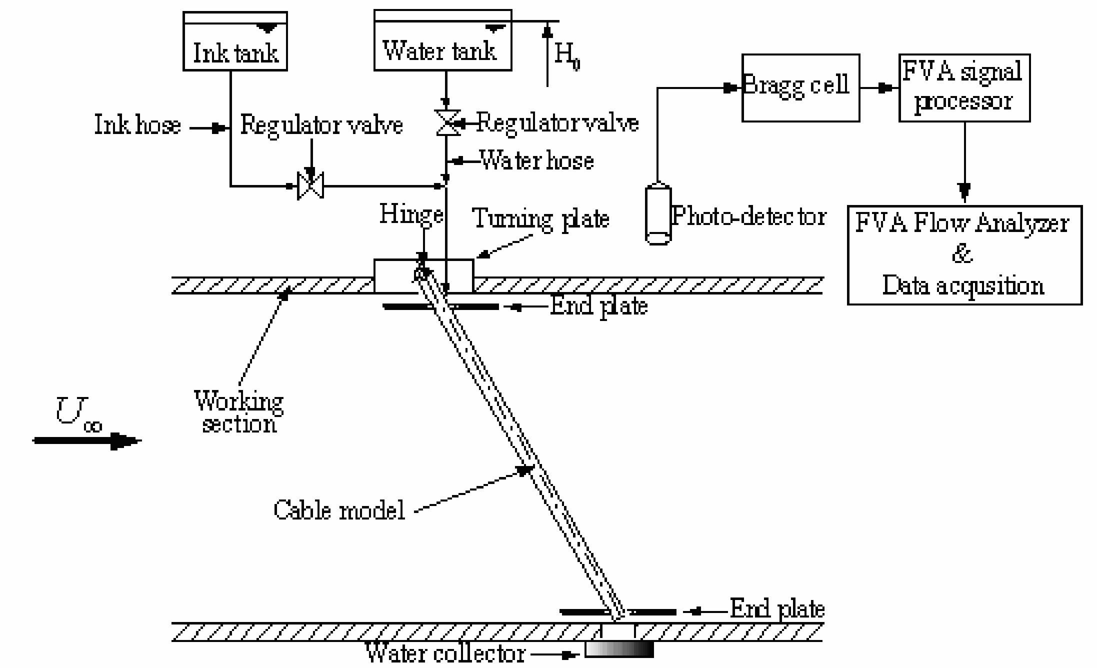

Figure 4.1 Schematic of experimental arrangement.

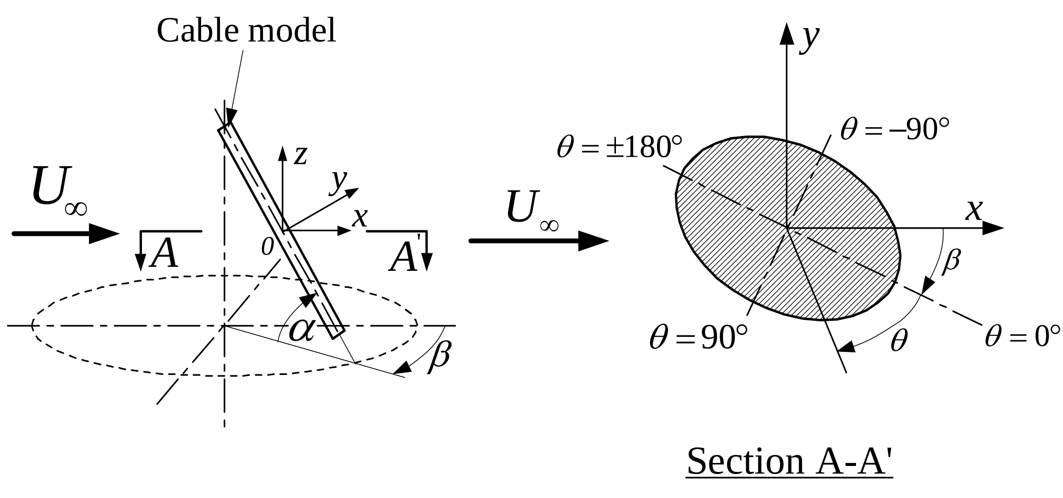

Figure 4.2 Definitions of inclination angle α, yaw angle β, circumferential angle θ, and the coordinates x, y and z. The origin of the coordinate system was defined at mid span of the cable axis.

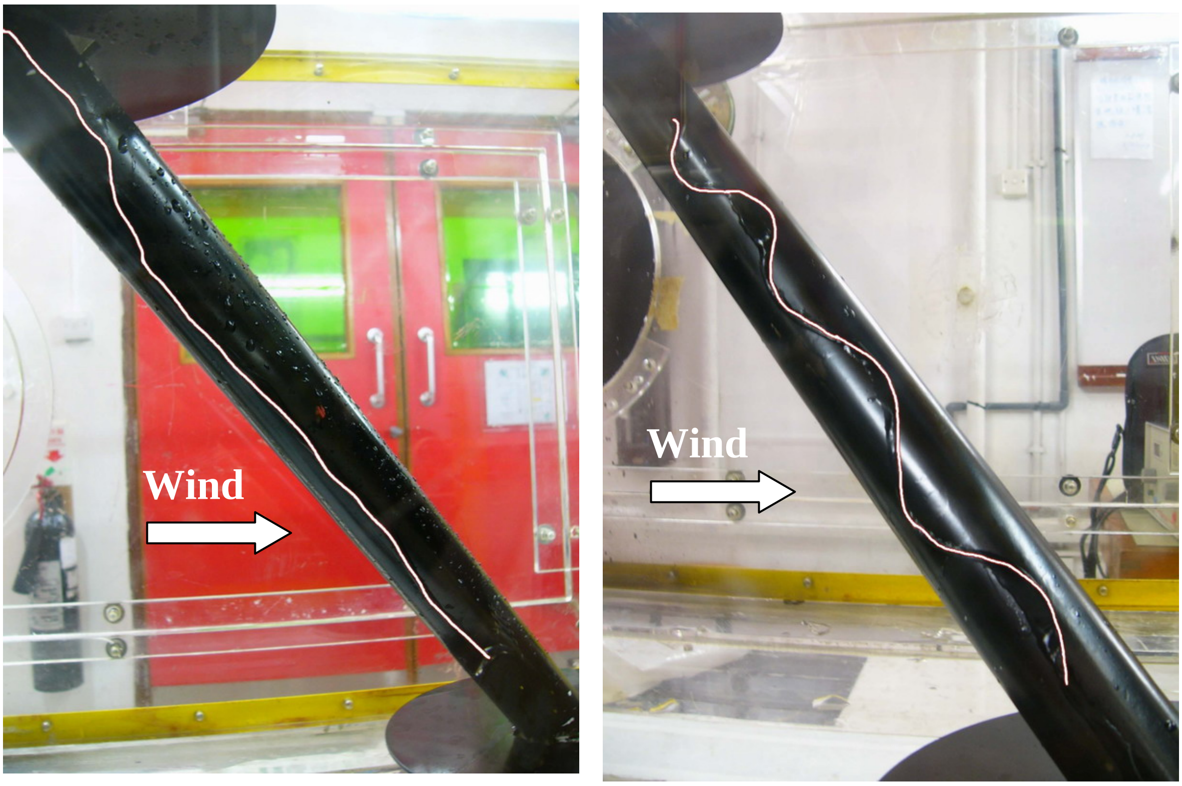

(a) (b)

Figure 4.3 Photos of water rivulets (white curves) on cylinder surface: (a) leeward rivulet, (b) windward rivulet.

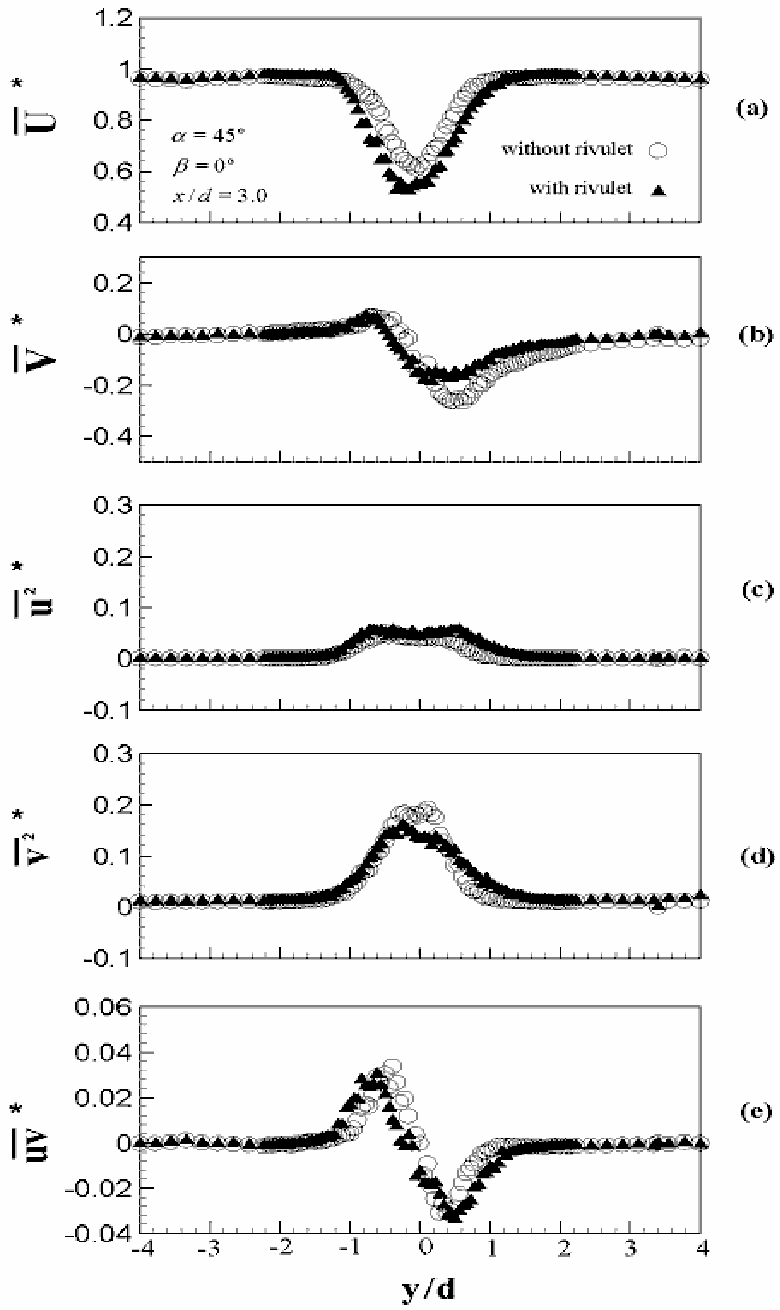

Figure 4.4 Cross-flow distributions of mean velocity, Reynolds normal stresses and shear stress at $\alpha = 45°$, $\beta = 0°$, x/d = 3.0: (a) $\overline{U}^*$, (b) $\overline{V}^*$, (c) $\overline{u^2}^*$, (d) $\overline{v^2}^*$, (e) $\overline{uv}^*$. ○, without rivulets; ▲, with two running water rivulets located symmetrically at $\theta \approx 110°$ and $\theta \approx -110°$.

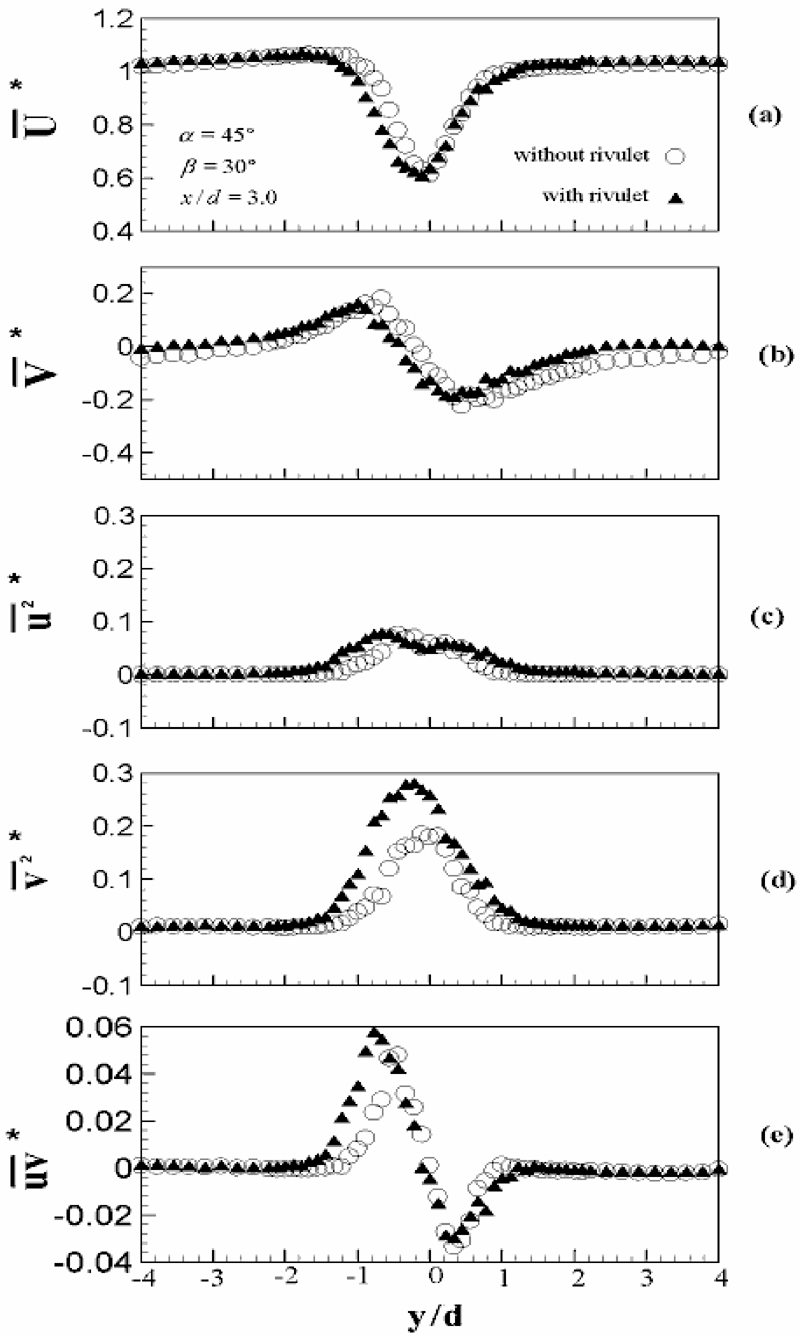

Figure 4.5 Cross-flow distributions of mean velocity, Reynolds normal stresses and shear stress at $\alpha = 45°$, $\beta = 30°$, x^* = 3.0: (a) $\overline{U}^*$, (b) $\overline{V}^*$, (c) $\overline{u^2}^*$, (d) $\overline{v^2}^*$, (e) $\overline{uv}^*$. ○, without rivulets; ▲, with a leeward running water rivulet at $\theta \approx 55°$ and a windward water rivulet at $\theta \approx -145°$.

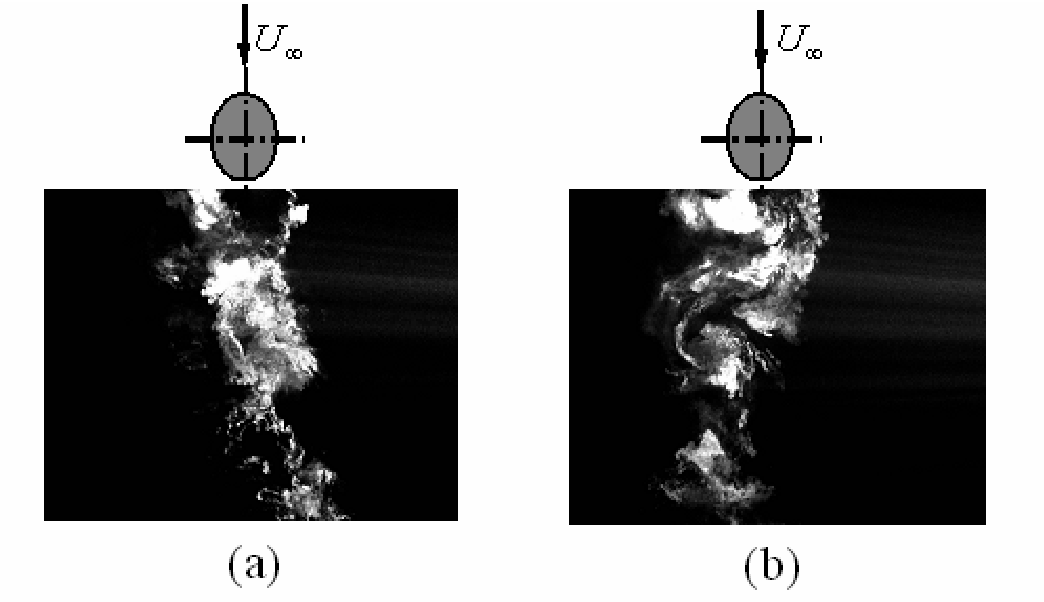

Figure 4.6 Typical flow patterns behind the inclined cylinder at $\alpha = 45°$, $\beta = 0°$ and *Re* = 27000 (U_∞ = 9 m/s) obtained in the wind tunnel in the horizontal (*x*, *y*) plane: (a) without water rivulet; (b) with two running water rivulets. Flow is up to down.

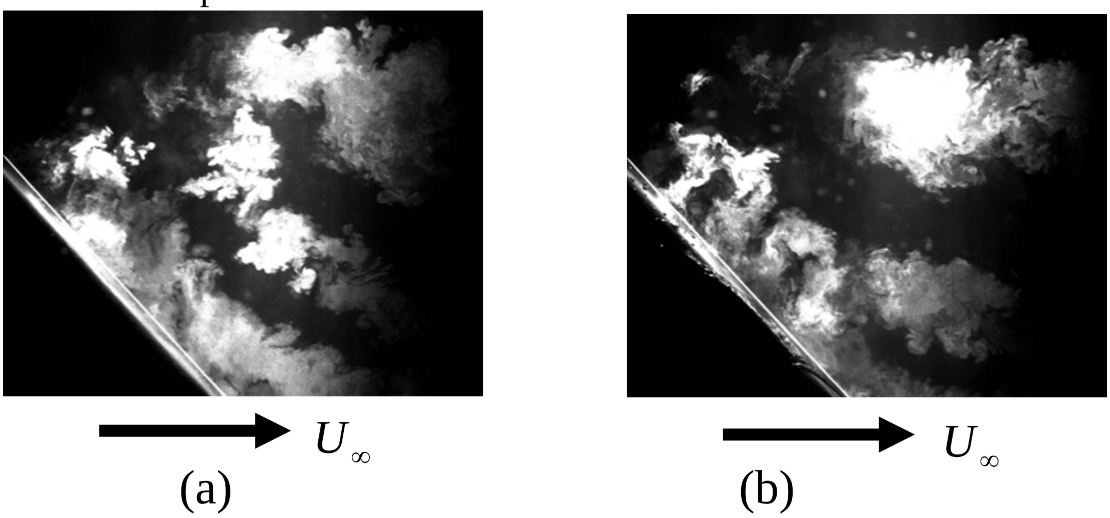

Figure 4.7 Typical flow patterns behind the inclined cable at $\alpha = 45°$, $\beta = 0°$ and *Re* = 27000 (U_∞ = 9 m/s) obtained in the wind tunnel in the vertical plane through the cylinder axis: (a) without water rivulet; (b) with two running water rivulets. Flow is left to right.

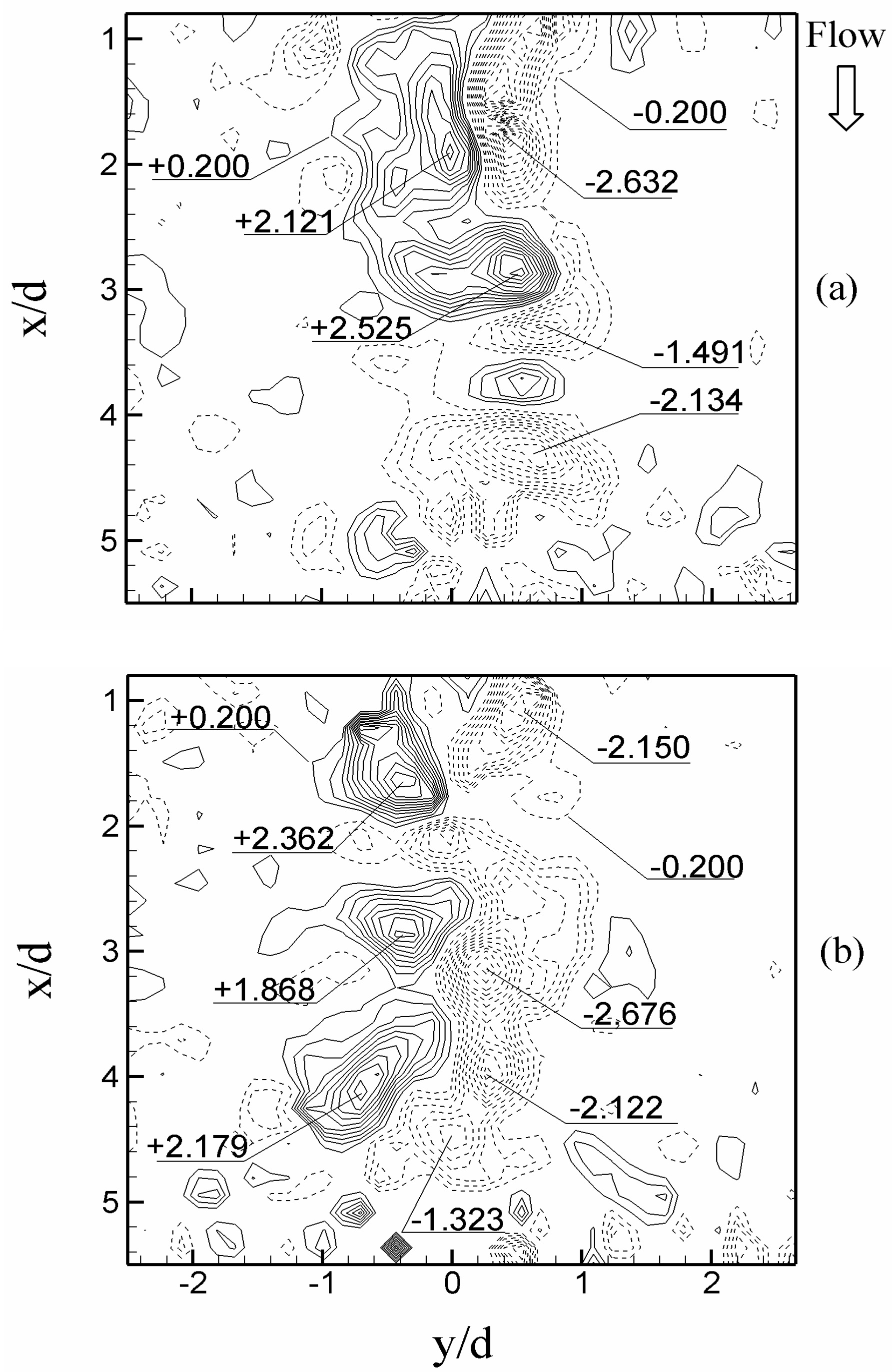

Figure 4.8 Instantaneous vorticity contours $\omega_z^* = \omega_z d / U_\infty$ obtained from PIV measurements at $\alpha = 45°$, $\beta = 0°$ and *Re* = 11400 (U_∞ = 9 m/s) in the horizontal (*x*, *y*) plane: (a) without water rivulet; (b) with two running water rivulets. Flow is up to down.

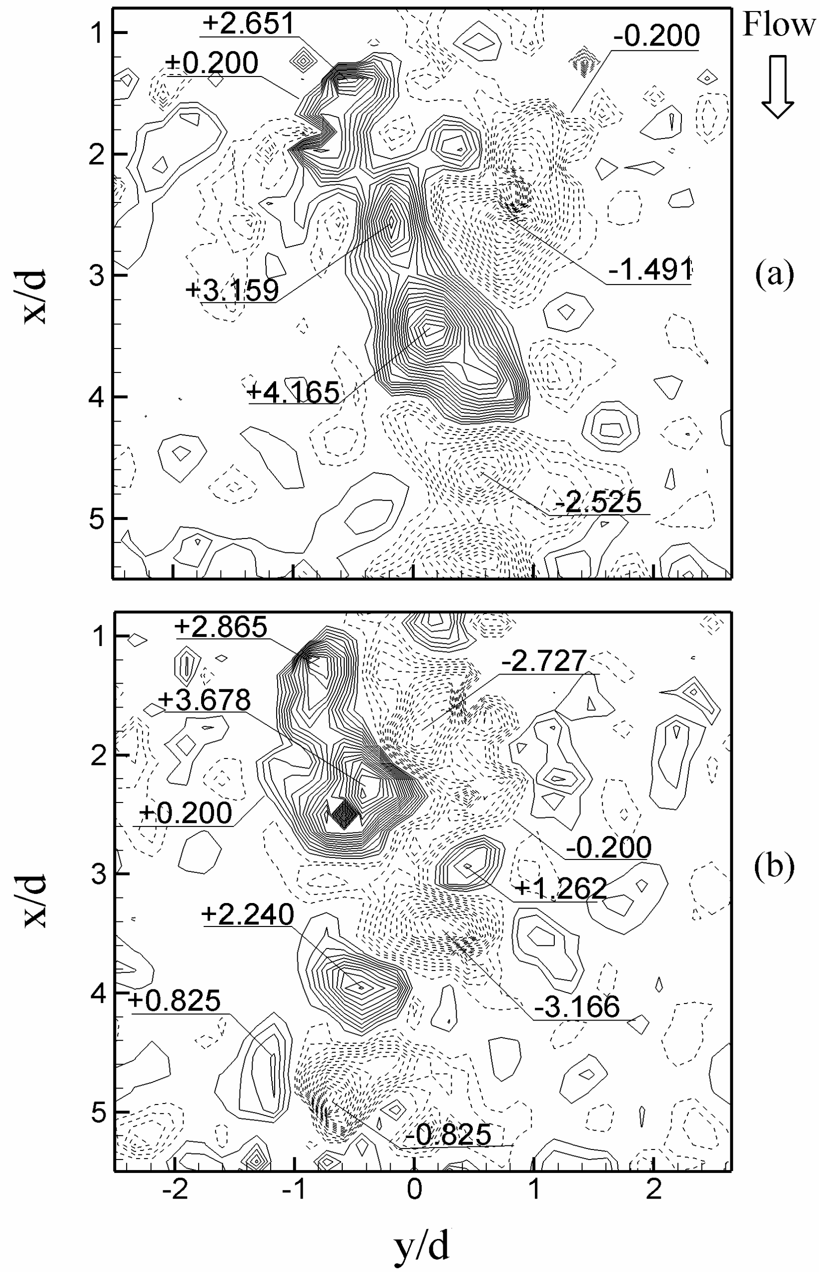

Figure 4.9 Instantaneous vorticity contours $\omega_z^* = \omega_z d / U_\infty$ obtained from PIV measurements at $\alpha = 45°$, $\beta = 30°$ and Re = 11400 (U_∞ = 9 m/s) in the horizontal (x, y) plane: (a) without water rivulet; (b) with two running water rivulets. Flow is up to down.

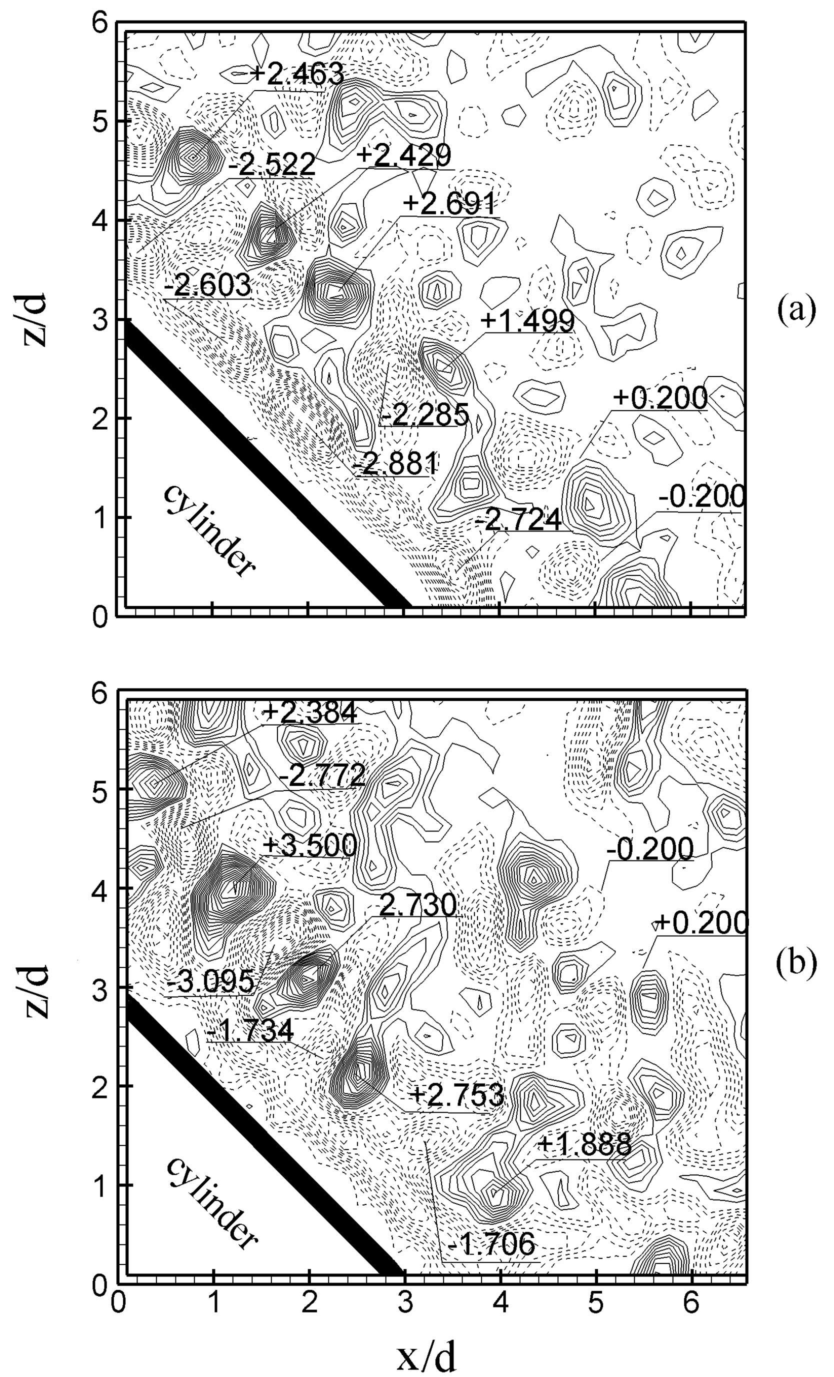

Figure 4.10 Instantaneous vorticity contours $\omega_y^* = \omega_y d / U_\infty$ obtained in a vertical plane through the cylinder axis from PIV measurements at $\alpha = 45°$, $\beta = 0°$ and Re = 11400 (U_∞ = 9 m/s): (a) without water rivulet; (b) with two running water rivulets.

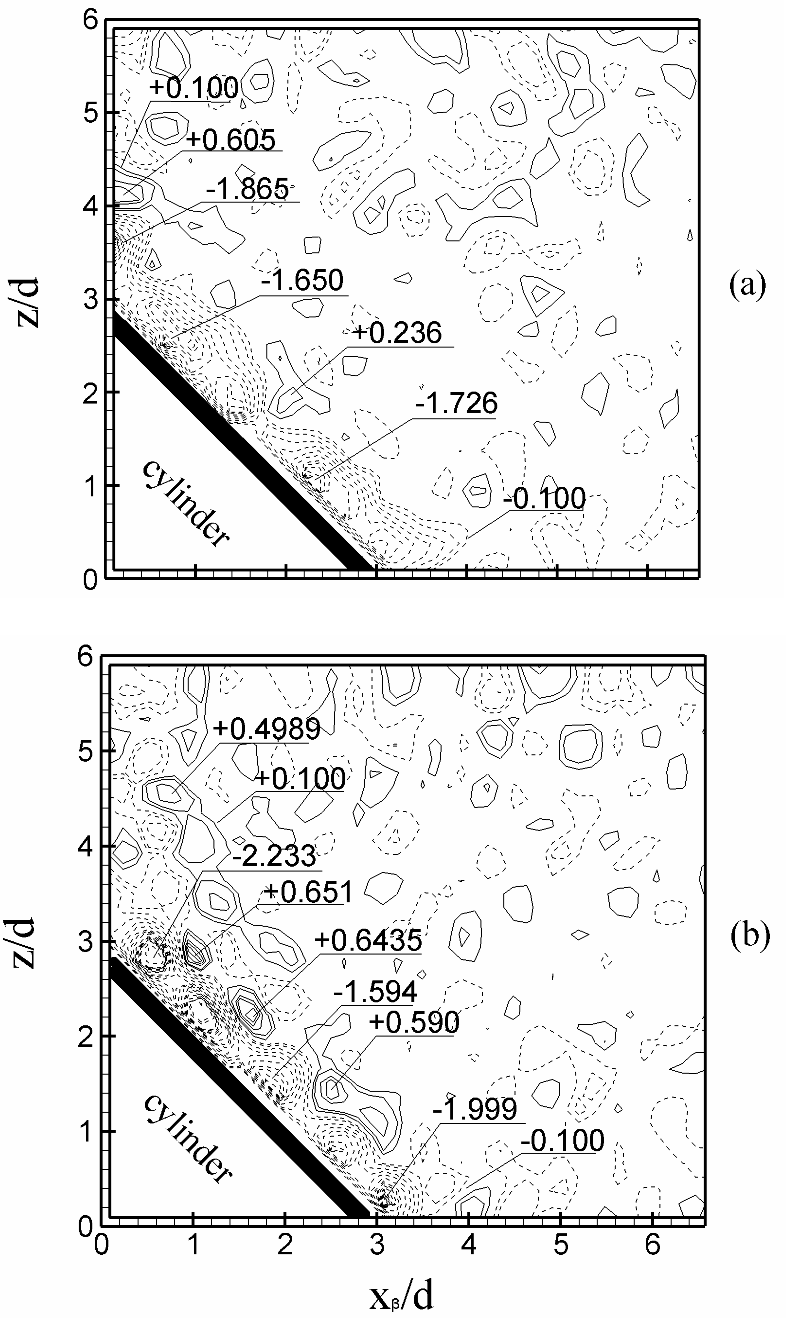

Figure 4.11 Instantaneous vorticity contours $\omega^* = \omega d / U_\infty$ obtained in a vertical plane through the cylinder axis from PIV measurements at $\alpha = 45°$, $\beta = 30°$ and *Re* = 11400 (U_∞ = 9 m/s): (a) without water rivulet; (b) with two running water rivulets.

Chapter 5: Conclusions and Recommendations

5.1 Conclusions

For a circular cylinder with symmetric cross-section and perpendicular to incoming flow, our three-dimensional PIV investigation of its near wake leads to the following conclusions.

The modified PIV technique, with one light sheet pre-displaced to another one, proves to be effective for the measurement of longitudinal structures in the near wake, at least up to $x^* = 20$, at a *Re* range of 2000 to 10000 where out-of-plane velocity component is high.

The longitudinal structures are different from spanwise vortices in size, strength and downstream evolution. Given a cut-off level of 10% of the maximum vorticity, the former has a dimension about one fifth that of the latter, while carrying a circulation about one sixth that of the latter. Whilst spanwise vortices break up at $x^* \approx 40$ (*e.g.* Zhou & Antonia 1993), it is difficult to detect the alternate arrangement of the positive and negative streamwise structures in the (y, z)-plane at $x^* > 15$.

An alternative definition for the vortex formation length is proposed based on the spanwise vortex growth in size. Under this new definition, the vortex formation length shrinks with increasing *Re* for the *Re* range investigated, qualitatively in agreement with former literature though determined length is however larger than that determined by the maximum streamwise fluctuating velocity (Bloor 1964).

The present measurement agrees with and complement with the data available in the literature in terms of the convection velocities, trajectory and strength of spanwise vortices in the near wake of a circular cylinder. Within the vortex formation length, the streamwise convection velocity of spanwise vortices increases from about 0.6 at $x^* = 3$ to 0.7 at $x^* = 5$ and, meanwhile, the lateral convection velocity drops approximately linear from 0.14 to near zero. With regard to vorticity, the maximum spanwise vorticity decays faster and linearly within the vortex formation region and slower beyond this region.

For an inclined circular cylinder with running water rivulets at sides, its effects on the near wake were experimentally investigated. The following conclusions may be drawn from the investigation.

The quasi-periodical vortex street occurs intermittently in the (x, y)-plane, and tends to occur more frequently in the presence of running water rivulets. The vortices may be anti-symmetrically or symmetrically arranged, unlike those behind a cylinder normal to the incident flow, which are predominantly anti-symmetric about the flow centreline. Nevertheless, the anti-symmetric vortex street occurs more frequently with running water rivulets than without. Meanwhile, there appear mushroom-like structures in the close proximity of the inclined cylinder in the (x, z)-plane, which are likely to result from the three-dimensional flow separation from the cylinder, that is, the separation line is pseudo-sinusoidal.

The vortex strength increases up to 60% as β changes from 0° to 30°. The result is consistent with the report that violent rain-wind-induced cable vibrations tend to occur for $\beta > 20°$. At $\beta = 30°$, the cross-stream distributions of the mean velocity $\overline{U}^*$, $\overline{V}^*$ and the Reynolds stresses $\overline{u^2}^*$, $\overline{v^2}^*$ and $\overline{uv}^*$ vary considerably in the presence of running water rivulets along the cylinder. Accordingly, the drag force on the cylinder, estimated based on $\overline{U}^*$, $\overline{u^2}^*$ and $\overline{v^2}^*$, increases significantly, compared with that in the absence of the rivulets. This increase and the violent rain-wind-induced vibration could be well connected. The formation of water rivulets on the cylinder surface increases appreciably the normalized dominant frequencies in the near-wake.

It is proposed that the large circumferential oscillation at large β of the water rivulets may act to perturb the flow separation from the cylinder. When the perturbation frequency that should be the same as the vortex shedding frequency coincides with the natural frequency of the fluid-cable system (or its harmonics), the system damping may be significantly reduced, and vortex shedding and hence structural vibration could be greatly amplified. This proposition has yet to be verified in future investigations.

5.2 Recommendations

The flow fields of fixed cylinder with or without rivulets are investigated in detail in this thesis. The following cases are worthy of future investigations with an elastically supported cylinder:

1. to achieve rain-wind induced vibration with a cylinder of diameter < 45mm in wind tunnel with real or artificial water rivulets.
2. the flow field around an elastically supported cylinder with real or artificial rivulets at various vibration phases, and the relationships between rivulet position and vibration amplitude, between free stream velocity and vibration amplitude, and between free stream velocity and Karman shedding frequency, deserve to be well studied.
3. effects of various natural frequencies, rivulets thicknesses and rivulet shapes on flow field and on the relationships mentioned in item 2.
4. time history for amplitude, shedding frequency, lift force *etc.* during the transition of cable states from an initially stationary to a full rain-wind induced vibration.

References

Achenbach, E. 1968 Distribution of local pressure and skin friction around a circular cylinder in a cross-flow up to $Re = 5\times10^6$. *J. Fluid Mech.* **34(4)**, 625-639.

Antonia, R.A., Rajagopalan, S. 1990 Determination of drag of a circular cylinder. AIAA Journal 28(10), 1833 – 1834.

Bearman, P.W., Owen, J.C. 1998 Special brief note - Reduction of bluff-body drag and suppression of vortex shedding by the introduction of wavy separation lines. *Journal of Fluids and Structures* **12(1)**, 123 – 130.

Bernal, L.P. and Roshko, A. 1986 Streamwise vortex structure in plane mixing layers. *J. Fluid Mech.* **170**, 499-525.

Bloor, S.M. 1964 The transition to turbulence in the wake of a circular cylinder. *J. Fluid Mech.* **19**, 290-309.

Bosdogianni, A., Olivari, D. 1996 Wind- and rain-induced oscillations of cables of stayed bridges. *Journal of Wind Engineering and Industrial Aerodynamics* **64**, 171-185.

Brede, M., Eckelmann, H. and Rockwell, D. 1996 On the secondary vortices in the cylinder wake. *Phys. Fluids* **8**, 2117-2124.

Cantwell, B. and Coles, D. 1983 An experimental study of entrainment and transport in the turbulent near wake of a circular cylinder. *J. Fluid Mech.* **136**, 321-374.

Chen, S.S. 1987 Flow-Induced Vibration of Circular Cylindrical Structures. Hemisphere Publishing Corporation, Washington.

Chyu, C. and Rockwell, D. 1996 Evolution of patterns of streamwise vorticity in the turbulent near wake of a circular cylinder. *J. Fluid Mech.* **320**, 117-137.

Den Hartog, J.P. 1956. Mechanical vibration, 4th ed., McGraw-Hill, New York.

Dwyer, H.A., Mccroskey, W.J. 1973 Oscillating flow over a cylinder at large Reynolds number. *J. Fluid Mech.* **61(4)**, 753-767.

Flamand, O. 1995 Rain-wind induced vibration of cables. *Journal of Wind Engineering and Industrial Aerodynamics* **57**, 353-362.

Gerrard, J.H. 1966 The three-dimensional structure of the wake of a circular cylinder. *J. Fluid Mech.* **25**, 143-164.

Gerrard, J.H. 1978 The wakes of a cylindrical bluff bodies at low Reynolds number. *Philosophical transactions of the Royal Society of London* **288**, 351-382.

Green, R.B. and Gerrard, J.H. 1993 Vorticity measurements in the near wake of a circular cylinder at low Reynolds numbers. *J. Fluid Mech.* **246**, 675-691.

Hama, F.R. 1957 Three-dimensional vortex pattern behind a circular cylinder. *J. Aeronautical Science* **24**, 156-158.

Hayakawa, M. and Hussain, F. 1989 Three-dimensionality of organized structures in a plane turbulent wake. *J. Fluid Mech.* **206**, 375-404.

Higuchi, H., Kim, H.J., Farell, C. 1989 On flow separation and reattachment around a circular cylinder at critical Reynolds numbers. *J. Fluid Mech.* **200**, 149-171.

Hikami, Y., Shiraishi, N. 1988 Rain-wind induced vibrations of cables in cable stayed bridges. *Journal of Wind Engineering and Industrial Aerodynamics* **29**, 409-418.

Hussain, A.K.M.F. and Hayakawa, M. 1987 Eduction of large-scale organized structures in a turbulent plane wake. *J. Fluid Mech.* **180**, 193-229.

Inoue, O. and Yamazaki, T. 1999 Secondary vortex streets in two-dimensional cylinder wakes. *Fluid Dyn. Res*. **25**, 1-18.

King, R., 1977 A review of vortex shedding research and its application. *Ocean Engineering* **4**, 141-171.

Lasheras, J.C. 1990 Three-dimensional vorticity modes in the wake of a flat plate. *Phys. Fluids* **A 2**, 371-380.

Lin, J.C., Vorobieff, P. and Rockwell, D. 1995a Three-dimensional patterns of streamwise vorticity in the turbulent near-wake of a cylinder. *J. Fluids Struct.* **9**, 231-234.

Lin, J.C., Towfighi, J. and Rockwell, D. 1995b Instantaneous structure of the near-wake of a circular cylinder: on the effect of Reynolds number, *J. Fluids Struct*, **9**, 409-418.

Mansy, H., Yang, P.M. and Williams, D.R. 1994 Quantitative measurement of three-dimensional structures in the wake of a circular cylinder. *J. Fluid Mech.* **270**, 277-296.

Matsumoto M., Shiraishi N., Shirato H. 1992 Rain-Wind induced vibration of cables of cable-stayed bridges. *Journal of Wind Engineering and Industrial Aerodynamics* **41-44**, 2011-2022.

Matsumoto, M., Saitoh, T., Kitazawa, M., Shirato, H., Nishizaki, T. 1995 Response characteristics of rain-wind induced vibration of stay-cables of cable-stayed bridges. *Journal of Wind Engineering and Industrial Aerodynamics* **57**, 323-333.

Matsumoto, M., Daito, Y., Kanamura, T., Shigemura, Y., Sakuma, S., Ishizaki, H. 1998 Wind-induced vibration of cables of cable-stayed bridges. *Journal of Wind Engineering and Industrial Aerodynamics* **74-76**, 1015-1027.

Matsumoto, M., Yagi, T., Shigemura, Y., Tsushima, D. 2001a Vortex-induced cable vibration of cable-stayed bridges at high reduced wind velocity. *Journal of Wind Engineering and Industrial Aerodynamics* **89**, 633-647.

Matsumoto, M., Yagi, T., Shigemura, Y., Tsushima, D. 2001b Rain-wind induced vibration of inclined cables at limited high reduced wind velocity region. In Proceedings of the Fifth Asia-Pacific Conference on Wind Engineering, Kyoto, pp.101-104.

Muchmore, B.B. and Ahmed, A. 1993 On streamwise vortices in turbulent wake of cylinders. *Phys. Fluids* **A5(2)**, 387-392.

Norberg, C. 1998 LDV-measurements in the near wake of a circular cylinder. *Publ. 87/2. Advances in understanding of bluff body and vortex induced vibration, Washington DC,* June 1998.

Ohshima, K. 1987 Aerodynamic stability of the cables of a cable-stayed bridge subject to rain (a case study of the Ajigawa bridge). In Proceedings of US-Japan Joint Seminar on Natural Resources, pp. 324-336.

Perry, A.E. and Steiner, T.R. 1987 Large-scale vortex structures in turbulent wakes behind bluff bodies. Part 1. Vortex formation. *J. Fluid Mech.* **174**, 233-270.

Persillon, H. and Braza, M. 1998 Physical analysis of the transition to turbulence in the wake of a circular cylinder by three-dimensional Navier-Stokes simulation. *J. Fluid Mech.* **365**, 23-88.

Prasad, A. and Williamson, C.H.K. 1997 Three-dimensional effects in turbulent bluff-body wakes. *J. Fluid Mech.* **343**, 235-265.

Ramberg, S.E. 1983 The effects of yaw and finite length upon the vortex wakes of stationary and vibrating circular cylinders. *J. Fluid Mech.* **128**, 81-107.

Sung, J. and Yoo, J.Y. 2003 Near-wake vortex motions behind a circular cylinder at low Reynolds number. *J. Fluids Struct.* **17**, 261-274.

Thomson, K.D., Morrison, D.F., 1971. The spacing, position and strength of vortices in the wake of slender cylindrical bodies at large incidence. *J. Fluid Mech.* **50**, 751-783.

Verwiebe, C., Ruscheweyh, H. 1998 Recent research results concerning the exciting mechanisms of rain-wind-induced vibrations. J*ournal of Wind Engineering and Industrial Aerodynamics* **74-76**, 1005-1013.

Wei, T. and Smith, C.R. 1986 Secondary vortices in the wake of circular cylinders. *J. Fluid Mech.* **169**, 513-533.

Wianecki, J. 1979 Cables wind excited vibrations of cable stayed bridge. In Proceedings of the 5th International Conference on Wind Engineering, vol. l.2, pp. 1381-1393.

Williamson, C.H.K. 1988 The existence of two stages in the transition to three-dimensionality of a cylinder wake. *Phys. Fluids* **31**, 3165-3168.

Williamson, C.H.K. 1995 Scaling of streamwise vortices in wakes. *Phys. Fluids* **7**, 2307-2309.

Wu, J., Sheridan, J., Soria, J. and Welsh, M.C. 1994a An experimental investigation of streamwise vortices in the wake of bluff body. *J. Fluids Struct.* **8**, 621-635.

Wu, J., Sheridan, J., Welsh, M.C., Hourigan, K., Thompson, M. 1994b Longitudinal vortex structures in a plane wake. *Phys. Fluids* **6**, 2883-2885.

Wu, J., Sheridan, J., Welsh, M.C. and Hourigan, K. 1996 Three-dimensional vortex structures in a cylinder wake. *J. Fluid Mech.* **312**, 201-222.

Xu, S.J., Zhou, Y., So, R.M.C. 2003 Reynolds number effects on the flow structure behind two side-by-side cylinders. *Phys. Fluids* **15**, 1214-1219.

Yamaguchi, H. 1990 Analytical study on growth mechanism of rain vibration of cables. *Journal of Wind Engineering and Industrial Aerodynamics* **33**, 73-80.

Yiu, M. W., Zhou, Y., Zhou, T. & Cheng, L. 2004 Reynolds number effects on 3-D vorticity in a turbulent wake, *AIAA J.* **42**, 1009-1016.

Yoshimura, T., Tanaka, T., Sasaki, N., Nakatani, S., Higa, S. 1988 Rain-wind induced vibration of the cables of the Aratsu Bridge. In Proceedings of the 10th National Conference on Wind Engineering, Tokyo, pp. 127-132.

Zhang, H.J., Zhou, Y. and Antonia, R.A. 2000 Longitudinal and spanwise vortical structures in a turbulent wake. *Phys. Fluids* **12**, 2954-2964.

Zhang, H.Q., Fey, U. and Noack, N.R. 1995 On the transition of the cylinder wake. *Phys. Fluids* **7**, 779-794.

Zhang, M.M., Cheng, L., Zhou, Y. 2004 Closed-loop-controlled vortex shedding from a flexibly supported square cylinder under different schemes. *Phys. Fluids* **16**, 1439-1448.

Zhou, T., Zhou, Y., Yiu, M.W., and Chua, L.P. 2003 Three-dimensional vorticity in a turbulent cylinder wake. *Expts. Fluids* **35**, 459-471.

Zhou, Y. and Antonia, R.A. 1993 A study of turbulent vortices in the near wake of a cylinder. *J. Fluid Mech.* **253**, 643-661.

Zhou, Y. and Antonia, R.A. 1994a Critical Points in a Turbulent Near-Wake, *J. Fluid Mech.* **275**, 59-81.

Zhou, Y., Antonia, R.A. 1994b Effect of initial conditions on structures in a turbulent near-wake. *AIAA Journal* **32**, 1207-1213.

Zhou, Y., Wang, Z.J., So, R.M.C., Xu, S.J., Jin, W. 2001 Free vibrations of two side-by-side cylinder in a cross flow. *J. Fluid Mech*. **443**, 197 – 229.

Zhou, Y., Zhang, H. J. & Yiu, M.W. 2002 The Turbulent Wake of Two Side-by-Side Circular Cylinders, *J. Fluid Mech*. **458**, 303-332.